2012-05-23

UV Visible Spectra Analysis of High Temperature Water Gas Shift Catalysts Made from Iron, Lanthanum, Copper, and Chromium Oxides

Jared C. Brown
Brigham Young University - Provo

UV Visible Spectra Analysis of High Temperature Water Gas Shift Catalysts Made from Iron, Lanthanum, Copper, and Chromium Oxides

Jared Brown

A thesis submitted to the faculty of
Brigham Young University
in partial fulfillment of the requirements for the degree of

Master of Science

Morris D. Argyle, Chair
W. Vincent Wilding
Bradley C. Bundy

Department of Chemical Engineering

Brigham Young University

June 2012

ABSTRACT

UV Visible Spectra Analysis of High Temperature Water Gas Shift
Catalysts Made from Iron, Lanthanum,
Copper, and Chromium Oxides

Jared Brown
Department of Chemical Engineering, BYU
Master of Science

Hydrogen is a vital component in several different chemical reactions as well as a potential fuel source for the future. The water gas shift (WGS) reaction converts CO and water to hydrogen and CO_2. The objective of this work is to first, characterize the potential benefits of the addition of lanthanum oxide (lanthana) to the iron-chromium-copper (Fe-Cr-Cu) oxide catalysts industrially used in high temperature water gas shift processes, and second, analyze these catalysts using in-situ UV-Visible spectroscopy. The benefits of each component in the catalyst are discussed as well as potential benefits from the addition of lanthana. Lanthana is a rare earth oxide that dramatically increases the surface area of the iron based WGS catalysts, and small concentrations of other rare earth oxides (i.e. cerium) have been shown to increase the rate of desorption of CO_2 from iron surfaces (Hu Yanping 2002). Lanthana has similar chemical properties to other rare earth oxides tested and has not been previously tested as an additive to the WGS catalyst. Therefore catalysts with 0, 1, 2, 5, 10, and 20 wt% lanthana were made via a co-precipitation method in order to measure changes in activity, physical stability, and thermal stability. Catalyst characterization techniques utilized include electron dispersive X-ray spectroscopy (EDX), temperature programmed reduction (TPR) with hydrogen, and nitrogen physisorption (BET). The kinetic analysis was performed utilizing both mass spectroscopy (MS) and gas chromatography (GC).

The addition of 1 wt% lanthana to the Fe-Cr-Cu catalysts increases WGS reaction rates of the catalyst at 425°C and 350°C, however the 0% La catalyst has the highest rates at 375°C and 400°C. The 0% La catalyst shows significant drop off in rate at 425°C, suggesting that the lanthana provides a small thermal stabilizing, i.e. the addition of lanthana prevents catalyst sintering at higher temperatures. Traditionally, chromia acts as the sole thermal stabilizer in these catalysts. The addition of large amounts of lanthana inhibits the chromia stabilizing effect, however small additions of lanthana appear to have an additional catalyst promotional effect without interfering with the chromia thermal stabilization. The increased WGS reaction rates at higher temperatures could allow for greater throughput of reactants in industrial settings. Higher concentrations of lanthana decrease the activity due to what is believed to be disruption of the chromia stabilizing effect as well as reduced amount of the active phase of catalyst.

In-situ UV-Visible analysis shows that the oxidation state of the iron in the catalyst has a direct correlation to the UV-Visible light absorbance of the surface of the iron catalyst. Extent of reduction is traditionally measured with a synchrotron which is significantly more expensive than UV-Vis spectroscopy. This study uses the more economical UV-Vis spectrometer to determine similar information. The lanthana doped catalysts show an over-reduction of iron during WGS conditions (i.e. rapid reduction of Fe_2O_3 to Fe_3O_4 and FeO).

Keywords: extent of reduction, water gas shift, lanthana, UV-visible spectroscopy

Table of Contents

List of Figures

List of Tables

Chapter 1 Introduction

1.1 Background

Hydrogen is a vital reactant in hundreds of applications in the chemical process industries, such as reducing oxidized metals, increasing the degree of saturation in fats and oils, reacting with nitrogen to form ammonia, producing nickel by the Sherritt Gordon Processes, and removing sulfur and nitrogen from petroleum (Ramachandran 1998). Also, as production technologies for hydrogen improve, the potential to convert to a hydrogen-based economy becomes more feasible. While the "hydrogen economy" is not expected to increase the demand for pure hydrogen for quite some time, if ever, the demand for chemical intermediate purity hydrogen continues to increase.

Production of chemical grade hydrogen presents several challenges. There is no hydrogen well or mine like there is for natural gas or coal. The hydrogen atoms need to be stripped off of hydrocarbons or water to produce the gas. Methane is the preferred source of hydrogen because it has the highest hydrogen to carbon ratio of any hydrocarbon. Two reversible reactions produce hydrogen from methane. First, steam methane reforming:

$$CH_4 + H_2O \leftrightarrow 3H_2 + CO \qquad (1)$$

is followed by the water gas shift to further oxidize the CO to form an additional hydrogen molecule:

$$CO + H_2O \leftrightarrow H_2 + CO_2 \qquad (2)$$

(Twigg 1989). Steam methane reforming, is highly endothermic ($\Delta H° = 206$ kJ mol^{-1}) and therefore equilibrium shifts towards hydrogen production if the temperatures are high and the pressures are low. Conversely, the water gas shift reaction is slightly exothermic ($\Delta H° = -41$ kJ mol^{-1}), meaning that hydrogen production is favored at lower temperatures. However, at these lower temperatures, the homogeneous water gas shift reaction proceeds too slowly for practical industrial production.

Methane is a valuable gas used in industrial and commercial heating applications. Methane steam reforming requires the use of this widely used fuel and steam, but produces a toxic gas, CO, with the desired H_2. The water gas shift reaction utilizes the poisonous CO and water to create a less harmful gas, CO_2, and more of the desired H_2. A significant challenge then to the mass production of H_2 is the tradeoff of kinetic rate versus low conversion of H_2 in the water gas shift reaction. To produce significant quantities of H_2, a catalyst is required to increase the rate of the forward water gas shift reaction.

The objective of this work is to characterize the potential benefits of the addition of lanthanum oxide (lanthana) to the iron-chromium-copper (Fe-Cr-Cu) oxide catalysts industrially used in high temperature water gas shift processes. Lanthana is a rare earth oxide that dramatically increases the surface area of the iron based WGS catalysts and small concentrations of other rare earth oxides (i.e. cerium) have been shown to increase the rate of desorption of CO_2 from iron surfaces (Hu 2002). Lanthana has similar chemical properties to other rare earth oxides tested and has not been previously tested as an additive to the WGS catalyst.

Exposure to WGS conditions reduces the active iron phase, Fe_3O_4, to FeO and eventually metallic iron. The longevity of the WGS catalyst is directly tied to the rate and the extent to

which this reduction occurs. Analyzing these catalysts using in-situ UV-Visible spectroscopy will provide insights into the extent of reduction of the catalyst during water gas shift conditions. The improved understanding of the catalytic mechanisms provided by the UV-Visible detection and the kinetic analysis that will also be performed will guide improvements to the activity and longevity of the catalyst(s).

Due to the low conversions at high temperatures, a staged process is used industrially to optimize H_2 output versus residence time. A high temperature water gas shift process utilizing iron oxides with chromium and copper promoters and a low temperature catalyst utilizing copper, zinc, and alumina oxides, and occasionally a series of precious metals (gold, platinum, etc.) are arranged in series. This study will focus on analyzing the high temperature shift (HTS) catalysts.

1.2 Iron Catalyst Properties

The iron oxide, specifically magnetite (Fe_3O_4) contains the active sites that facilitate the forward water gas shift reaction (Sato 2004). A study by Sato et al. showed that non-catalytic water gas shift done under supercritical conditions has a reaction rate roughly 10^7 times smaller than with catalytic iron at non-supercritical temperatures (Sato, Takafumi 2004). This suggests that the use of a catalyst is of the utmost importance in improving H_2 production.

While the water gas shift reaction (WGS) on iron oxide is significantly better than non-catalytic WGS, there are some challenges to using this catalyst. Iron oxides are somewhat resistant to both sintering and various potential poisons; however, there is still a decline in catalytic activity with time (Chinchen 1984). The activity of a catalyst is strongly dependent on surface area of the catalyst. Chinchen et al. explain that there are two stages to activity reduction

in iron oxide catalysts. First, there is an initial fast decay of activity that resolves to a pseudo steady state activity. Secondly, a slow decline of steady state activity is due to sintering, the loss in surface area accompanying a growth in mean pore size due to mobility of the catalytic surface structures at high temperatures (Chinchen 1984).

Both the rapid and slow decays of activity have been attributed to a form of sintering (Chinchen 1984). Therefore, one way to improve the water gas shift reaction rate is to decrease both the amount and rate of sintering, thus increasing the effective activity of the catalyst over an extended period of time. The other method for improving water gas shift catalyst performance involves increasing the intrinsic activity of the catalyst being used.

1.3 Water Gas Shift Reaction over Iron

The WGS reaction can be modeled fairly accurately using a power law equation developed by Podolski and Kim of the form

$$R = k\, P_{CO}^{a}\, P_{H2O}^{b}\, P_{CO2}^{c}\, P_{H2}^{d}\, (1-\beta) \qquad (3)$$

where, R = reaction rate (mol gcat $^{-1}$ s^{-1}); P_i = partial pressure of reactant, i; a, b, c, d = reaction order of CO, H_2O, CO_2, and H_2, respectively; k = rate constant = $A \exp(-E/R'T)$; R' = universal gas constant (kJ mol^{-1} K^{-1}); A = pre-exponential factor (mol g_{cat}^{-1} s^{-1}atm$^{-a-b-c-d}$); E = activation energy (kJ mol^{-1}); T = reaction temperature (K); and β is defined as

$$\beta = K^{-1}\, P_{CO}^{-1}\, P_{H2O}^{-1}\, P_{CO2}\, P_{H2} \qquad (4)$$

where K is the equilibrium constant (Hla 2009). Two standard industrial iron chromia copper oxide catalysts, HTC1 and HTC2 were used by San Shwe Hla in order to determine rate law data for the WGS reaction over Fe-Cr-Cu oxide catalysts. HTC1 has more chromia and less copper

than HTC2. (The importance of copper and chromia in the catalysts will be discussed in sections 1.5 and 1.7 respectively).

These catalysts were then analyzed for their kinetic production of H_2 under a variety of conditions to determine the power-law coefficients. Various compositions of feed gas were tested to produce the following results, which show the CO conversions for a series of reactor and catalysts (Figure 1).

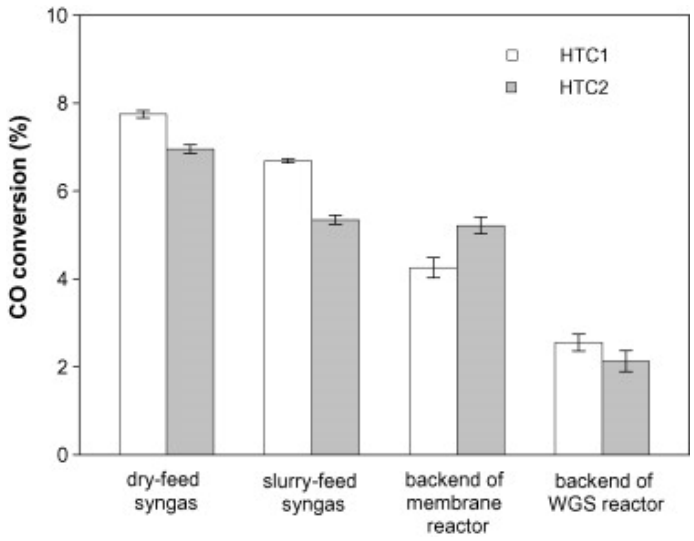

Figure 1 Conversion of CO over two iron based WGS catalysts at different feed conditions (Hla 2009).

The inlet CO concentration decreases from left to right for the four conditions listed in Figure 1, from 65% to 44%, 7%, and 4%, respectively. As shown, feed conditions as well as compositions of the iron based catalysts determine conversion of CO in the WGS reaction. These data were then used to calculate the desired power-law coefficients shown in Table 2.

Table 1 Kinetic results of power law fit 95% confidence interval (Hla 2009)

	a [CO]	b [H_2O]	c [CO_2]	d [H_2]	A	E(kJ mol^{-1})
HTC 1	1.0 ± 0.031	0	-0.36 ± 0.043	-0.09 ± 0.007	700 ± 50	111 ± 2.63
HTC 2	0.9 ± 0.041	0.31 ± 0.056	-0.156 ± 0.078	-0.05 ± 0.006	4.557 ± 0.133	88 ± 2.18

These data suggest that the equilibrium conversion of CO increases as the concentration of CO increases. However, at the same space velocity in each case, the efficiency of the process decreases with increasing concentration. For example, the highest CO conversion was shown in Figure 1 to be roughly 8% of the 65 mol% CO composition feed gas. The amount of excess un-reacted CO remaining is still nearly 60 mol% of the exit stream.

The following sections will discuss the non-iron components of the catalyst. Each component's known benefits, as well as the potential benefits of the new additive lanthana, will be explained.

1.4 Ceria and Lanthana

In addition to previously discussed shortcomings, two other problems with using iron-chromium oxides are chromium (VI) can be toxic and under certain conditions these catalysts can enhance methanation or Fischer-Tropsch reactions and thus catalyze the formation of hydrocarbons, reducing the amount of H_2 produced from the system (Hu 2000). An alternative to using solely chromia is to use a combination of less chromia with some ceria (cerium oxide); a relatively more expensive lanthanide that has been shown to store and release H_2 and O_2 from catalyst surfaces (Hu 2000). Ceria is currently being used in ammonia synthesis processes that use catalysts similar to those used in WGS. One catalyst under investigation is Fe-Ce-Cr-O; this catalyst provides the stability of the chromia, but uses less chromia than the industrial standard, while the ceria enhances the ability for adsorbed oxygen species, like H_2O and CO, to desorb

from the catalyst surface. Pure ceria reacting with CO_2 can create undesired products under WGS conditions. However, in the Fe-Ce-Cr-O catalyst, the ceria forms intermetallic M-Ce compounds that facilitate CO desorption on the catalyst surface (Hu 2000).

Therefore, ceria addition to the catalyst can improve desorption of adsorbed species, reduce use of potentially toxic chromium oxide, and reduce the reduction temperature necessary in catalyst activation. This study used lanthana, a similar lanthanide oxide to ceria, but with slightly different properties, to determine if the benefits of the ceria additive in the iron-chromia-ceria catalyst are also present in an iron-chromia-lanthana catalyst; and if these benefits, such as increased surface area and better oxygen desorption rates, are enhanced with lanthana compared to ceria. Further, ultraviolet-visible (UV-Vis) spectroscopy was used to probe the oxidation state of the catalysts to provide mechanistic insight on the catalysis.

1.5 Copper in Water Gas Shift Catalysts

The inclusion of 4 wt% CuO in the Fe_3O_4/Cr_2O_3 catalysts has been shown to reduce the activation energy 25-27% for the WGS reaction (Rhodes 2003). This reduction in activation energy was originally explained through metal Cu sites increasing the reducibility of the catalyst; however, XRD shows that the CuO maintains a solid solution, meaning that the Cu is still bonded in the lattice with the Cr and Fe and not as its own structure of metallic Cu, with the iron-chromia base. Therefore no Cu metal is present (Rhodes 2003). TPR data from this study is shown Figure 2.

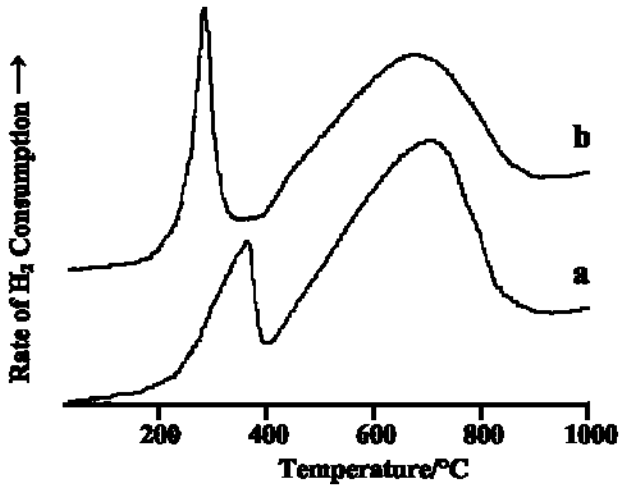

Figure 2 Temperature programmed reduction of catalyst precursors using 5% H_2 in Ar showing H_2 consumption with increasing temperature: (a) Fe_3O_4/Cr_2O_3; (b) $CuO/Fe_3O_4/Cr_2O_3$.

Therefore, the addition of the copper decreases the peak temperature from about 375°C tot 300°C suggesting, that less energy is required to reduce the catalyst. This is then manifested in a reduction of activation energy from 110 (kJ mol^{-1}) to 80 (kJ mol^{-1}). The copper also acts as a stabilizer of the CO reduction process; meaning that the iron-chromia catalyst is more readily reduced by CO because of the addition of the copper oxide to the system. This is shown in Figure 3 (Rhodes 2003).

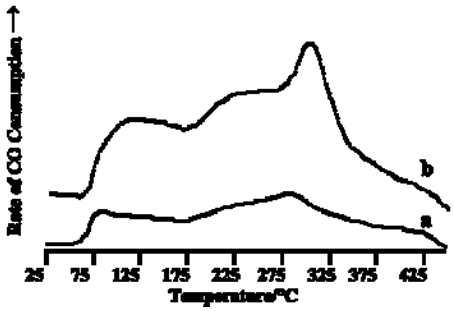

Figure 3 Temperature programmed reduction of catalyst precursors using 5% CO in He showing CO consumption with increasing temperature: (a) Fe_3O_4/Cr_2O_3; (b) $CuO/Fe_3O_4/Cr_2O_3$.

This suggests that higher concentrations of CO can be added to the system and still achieve the desired oxidation of the CO, potentially increasing throughput of WGS reactants in an industrial process.

1.6 Structural Stability of Iron Catalysts in WGS Conditions

Fe_3O_4 particles under WGS conditions have a tendency to agglomerate, forming large particles of iron crystals. Rethwisch et al. explains that upon adding water to the gases being fed to the magnetite catalyst, the iron begins to form clusters of particles. As these clusters form, they become larger and further apart from each other, making it difficult for the particles to continue to agglomerate past a certain size. This mobility of iron particles could be caused by hydroxylation of the magnetite surface (Rethwisch 1985). In other words, as the water binds to the surface of the magnetite forming an intermediate Fe_3O_4-H + HO, the hydrogen on the surface can hydrogen bond with the excess water in the gas system, allowing for mobility of the iron particle. TEM images taken by Rethwisch are shown in Figure 4 (Rethwisch 1985).

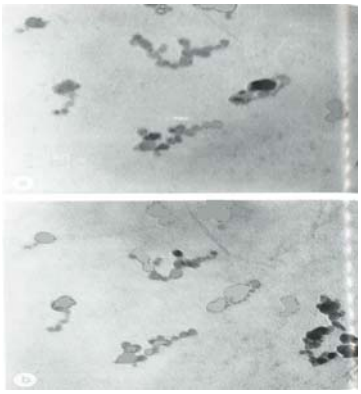

Figure 4 Transmission electron micrographs of Fe_3O_4 particles on cleaved single crystal graphite. (a) same sample as (b) treated an additional 24 h in CO/CO_2 (15/85) at 660 K (b) same field of view after an additional 24 h in $CO/CO_2/H_2O$ (32/4/64) at 660K (Rethwisch 1985).

Note how the darker areas, or areas of highest Fe_3O_4 concentration, in the upper image have come together to form a large cluster of darker particles in the lower right corner of the lower image. It is because of this agglomeration of magnetite particles that a stabilizer must be added to the catalyst to maintain as many active sites as possible during the WGS reaction.

1.7 Effects of Chromia in WGS Catalysts

Traditional WGS catalysts include roughly 8% by weight of Cr_2O_3. A study by Doppler et al. suggests that due to the aforementioned agglomeration, "a significant fraction of the surface area is then contained within the pore structure of the clusters of particles … and that the surface area within these pores would no longer be accessible, especially in the presence of water." (Doppler 1988). Doppler's study involved taking three catalysts (Fe_3O_4, $Fe_{2.75}Cr_{0.25}O_4$, and $Fe_{2.5}Cr_{0.5}O_4$) and measuring the decrease in surface area with time. The decreases were 0.17, 0.15, and 0.05 ($m^2\ gcat^{-1}\ h^{-1}$), respectively. Traditional WGS catalysts have surface areas around 40 m^2/gram, so the catalysts would lose 90% of their original surface area in 9 days, 10 days, and 30 days respectively. Thus, as the Cr concentration increased, the reduction in overall surface area caused by agglomeration decreased.

Many catalysts have been evaluated using Temperature Programmed Reduction (TPR) sequences to determine the stabilizing effect of chromia. The data in Figure 5 are from a study by Gunugunuri et al. (Gunugunuri 2011).

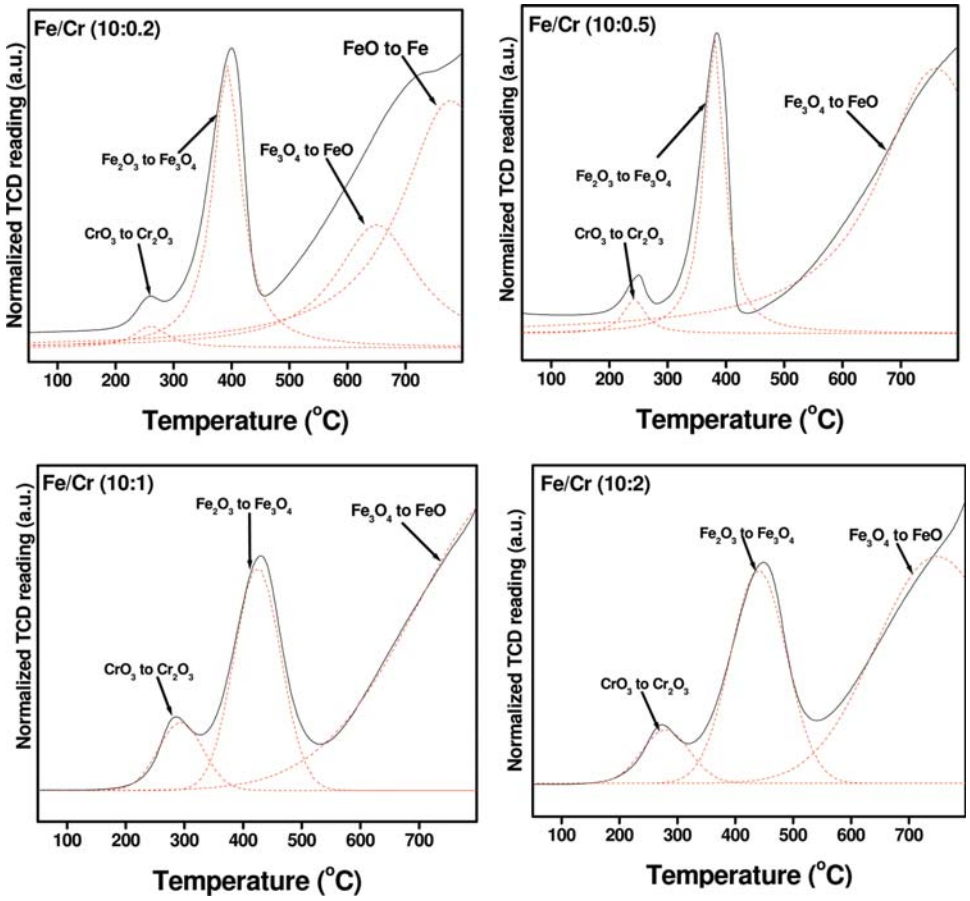

Figure 5 TPR data of multiple compositions of iron chromia catalysts performed by (Gunugunuri 2011).

The data in Figure 5 show that as the concentration of Cr is increased the peak temperature at which the Fe_2O_3 to Fe_3O_4 reduction takes place increases. This suggests that additional energy is required to reduce the catalyst, and therefore there is additional structural stability of the catalyst. While an increase in activation energy usually denotes a decrease in activity, this is an activation energy increase in the reduction of the catalyst with hydrogen, not in the water gas shift reaction. This is additionally beneficial in that the added chromia inhibits the reverse reaction. There was not, however, a significant change in the activation energy of the water gas shift reaction with the addition of the chromium oxide.

The added stability given by the chromia is largely credited to the spinel structure formed with iron. Figure 6 shows a crystal structure for an iron chromium spinel, with the iron in the tetrahedral sites and the chromium in the octahedral sites. This structure provides added stability by increasing the number of bonds between oxygen atoms and surrounding cations. The picture on the left represents normal magnetite, while the picture on the right shows the added bonds of the spinel structure. The iron is able to form octahedral connections to the oxygen atoms, while the chromium takes the original octahedral positions of the magnetite structure.

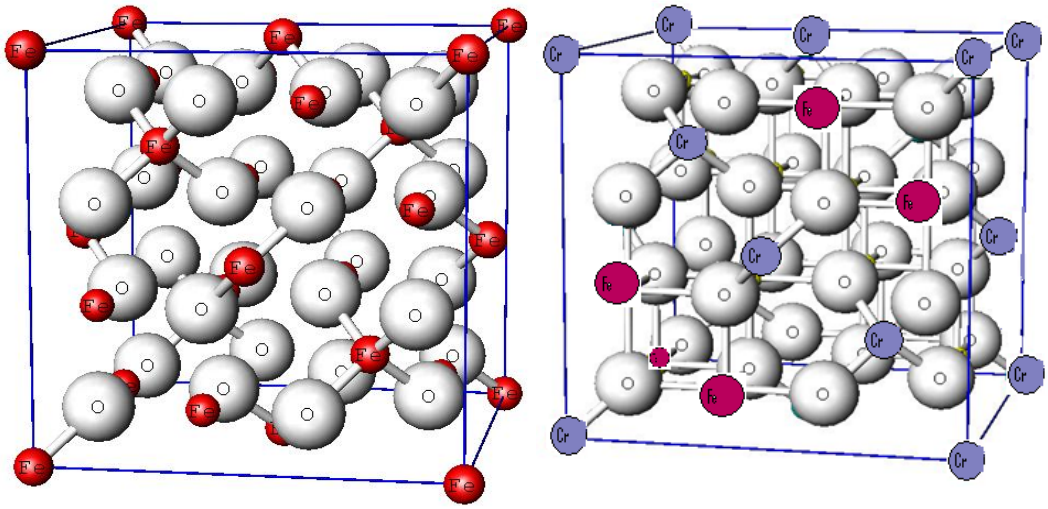

Figure 6 Spinel structure adopted by XY_2O_4 oxides. In the normal spinel structure ($FeCr_2O_4$), tetrahedral sites are occupied by divalent cations such as Fe^{2+} and octahedral sites are occupied by trivalent cations such as Cr^{3+} (Sherman 2008).

In industry, water gas shift catalysts are traditionally pre-treated in 10% water at 400°C for several hours to create this spinel structure before being placed into water gas shift conditions. In this study, the spinel is formed over time as water is introduced during the water gas shift process. This is done to reduce complexity in the water gas shift experimental design.

Chapter 2 Characterization and Kinetic Results

2.1 Introduction

This chapter will explore the kinetic data obtained using various lanthana-containing catalysts, as well as describe characterization techniques utilized.

2.1.1 Laboratory Set-Up

A temperature programmed surface reactor (TPSR) was built for the kinetic studies. The TPSR includes a furnace for the reactor, a temperature controller, mass flow controllers, and syringe pumps for metering water into a steam generator. An Agilent 7890 Gas Chromatograph (GC) was used to take the WGS kinetic data. An MKS Cirrus 100 mass spectrometer was used to make kinetic measurements during the UV-visible experiments. Figure 7 shows the flow diagram for the experimental apparatus. All lines from the mass flow meters to the kinetic reactor were wrapped in heat tape maintained at 150°C to avoid water condensation.

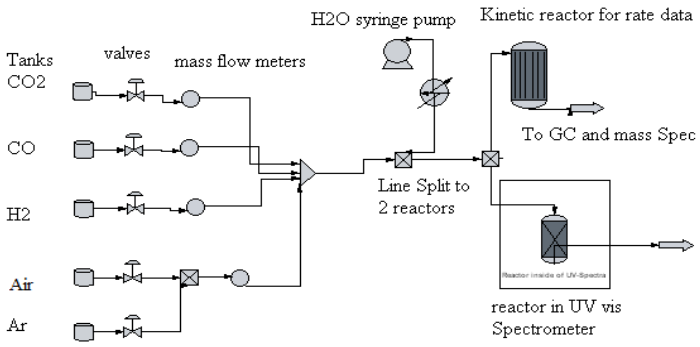

Figure 7 Lab experimental apparatus

2.1.2 Experimental Assumptions

This system is designed to be a differential reactor to avoid mass and heat transfer limited regimes, as well as to limit the reverse reaction. The differential reactor assumption can also reduce the difficulty of reactor modeling to simple algebraic analysis, similar to that used with a CSTR. However, due to the reverse WGS reaction, the method of initial rates was implemented to determine the initial forward rate of reaction.

The method of initial rates involves measuring the rate for a given initial concentration of CO. The reactant flow rate is varied to obtain several (3-4) different CO conversions that ideally are less than 5%. A plot of CO conversion rate versus inverse flow rate is made and a best fit line is extrapolated back to infinite flow (zero conversion) conditions. The y-intercept is taken as the initial rate for that specific initial CO concentration. The process is repeated several times at various initial CO concentrations until a log-log plot of initial rates versus initial concentrations can be made, the slope of which is the reaction order for rate law of the catalyst. Repeating this process at different temperatures permits determination of activation energies (via the Arrhenius equation), as well as other kinetic data.

2.1.3 Catalyst Characterization

Catalyst characterization techniques employed in this study were surface area analysis, temperature programmed reduction (TPR), temperature programmed oxidation (TPO), and Energy Dispersive X-Ray Spectroscopy (EDX).

2.1.4 BET Surface Area Analysis

Nitrogen physisorption, commonly called BET (Brunauer, Emmett, and Teller) analysis involves physical adsorption to measure total surface area of the catalysts. Nitrogen gas at the

normal boiling point of liquid nitrogen (77 K) is absorbed by the catalyst. The BET method analyzes the amount of nitrogen adsorbed by the catalyst as a function of the added pressure of nitrogen. A typical isotherm is shown in Figure 8 (Sinfelt 2002).

Figure 8 Traditional BET isotherm of nitrogen adsorption near 77 K (Sinfelt 2002).

The problem with this type of adsorption is that eventually more than one layer of adsorbate begins to form. These additional adsorbed species above a monolayer of coverage no longer represent the exterior surface area of the catalyst. Brunauer, Emmett, and Teller determined that the initial monolayer of adsorption occurred in the fairly linear region, between 5 and 35%, of the pressure scale shown in Figure 8 (Sinfelt 2002).

2.2 Experimental Methods

This section describes the equipment used, and the methodology of the kinetic data gathering process.

2.2.1 Gas Chromatograph

An Agilent 7890 gas chromatograph (GC) was used to determine the relative amounts of compounds in a gas stream. The carrier gas for this GC was helium (Airgas® 99.997) and a

thermal conductivity detector (TCD) was used. The column used was a packed column of length 2m outer diameter of 1/16 inches and an 80/100 Carboxen® type packing. The runs were done at a starting temperature of 24°C and increased to 225°C at a rate of 20°C/min.

Figure 9 shows a GC trace for a 1wt% LaO_x catalyst after 5 days of WGS conditions. Each of the three compounds being measured, H_2, CO, and CO_2 (water is removed prior to the GC by a desiccant bed) has a specific time at which it elutes from the column. Hydrogen comes out first at approximately the 1 minute mark, CO at 3.7 to 4 min. and CO_2 at 9 to 9.5 min.

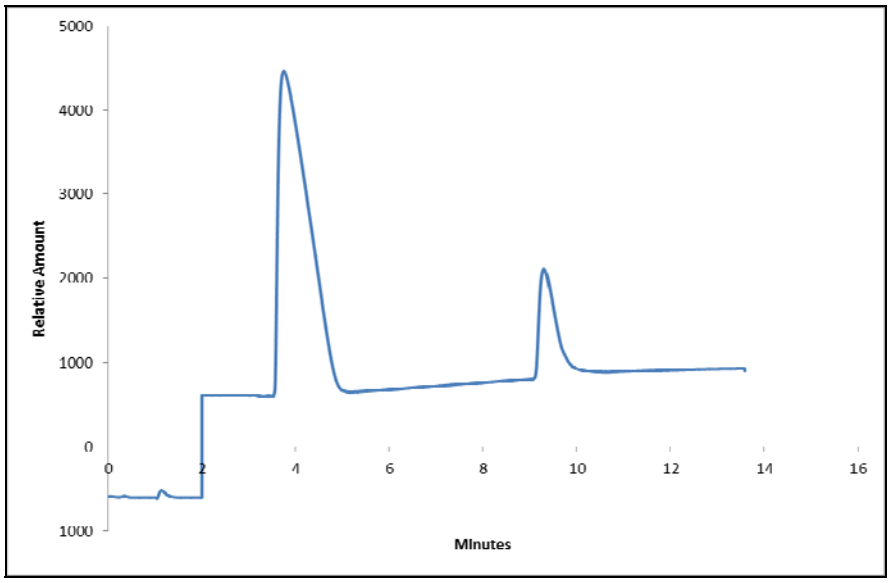

Figure 9 1 wt% lanthana catalyst GC reading after 5 days WGS conditions.

The area under each of these peaks cannot be directly related to a concentration of these elements without proper calibration. In this case, various known mixtures of CO and CO_2 were sent through the column and their relative peak areas measured. Using these peak areas for known concentrations, the various compositions of CO and CO_2 were obtained for WGS

conditions and converted to molar production of CO_2. These data can be converted into WGS rates and conversions for each catalyst, as shown in Section 2.3.3.

2.2.2 Mass Spectrometer

Mass spectroscopy involves ionizing gaseous compounds in a vacuum chamber and then measuring the mass to charge ratio of the ionized particles. As a sample is taken continuously over an extended period of time, there is an amount of residual particles that can cause an increase in effective concentration in the system, which is manifested by a drift in the signal with time. This "baseline drift" causes the baseline for the peaks to increase or decrease slightly over time, based on the accumulation or removal a compound from the system.

The output of this mass spectrometer is an electronic signal of the mass/charge (m/z) ratio for each species. This value, translated to a partial pressure in the vacuum chamber, directly correlates to concentration in the system, but still requires a calibration similar to the GC. An example of this is shown in Figure 10. The initial hydrogen concentration is 5% H_2 and 95% Ar. The mixture is then stepped down to 4%, 3%, 2%, and then back up to 5% H_2. The calibration graph shows how the change in concentration between these percentages is linear, therefore a direct correlation between the MS output and the real concentration in the line can be made. In section 3.3.2 TPR and TPO Analysis via Mass Spectrometer, a baseline of hydrogen is shown with a positive slope, this entire baseline can be assumed to be equal to the inlet 5% H_2 concentration sent into the system, because this calibration graph is linear.

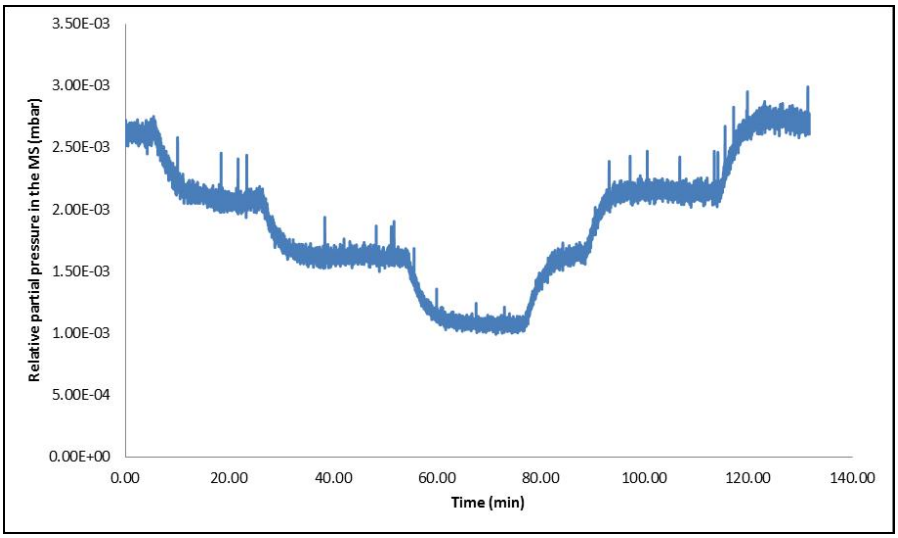

Figure 10 Hydrogen calibration for the mass spectrometer.

2.2.3 Temperature Programmed Surface Reactor

The WGS reaction (Equation 2) takes CO and H_2O and produces CO_2 and H_2. All four of these components are shown in Figure 7 as inlets into the reactor system. The CO_2 will be used for future analysis of reverse reaction effects on the reaction rate and was not used in this study. The H_2 and air were both used in the temperature programmed reduction (TPR) and temperature programmed oxidation (TPO) process steps. Water is added to the system via an ISCO 260D syringe pump at a steady rate of 0.05 sccm into a boiler held at 350°C. The steam then combines with the rest of the inlet gases that are pre-heated to 150°C and sent to a temperature programmed surface reactor (TPSR) at 400°C. The TPSR consists of a cylindrical furnace in which a quartz reactor tube is inserted. The tube never makes direct contact with any of the surface walls. The insertion point of the tubing is insulated with quartz wool to ensure an even temperature distribution throughout the quartz tubing. A thermocouple is inserted in a small dimple in the bulb that holds the catalyst in order to get a temperature reading as close to the

surface of the catalyst as possible without putting a hole in the quartz. This reactor tube contains a quartz frit inside of the bulb in the quartz tubing to hold the catalyst in place during the reaction.

Following the TPSR are two systems designed to remove water from the product gases. The first is a flash tank roughly 18 in. long and 3 in. in diameter maintained at ambient conditions. The second is a desiccator column of similar dimensions filled with a calcium sulfate (Dri-rite®) desiccant. The water is extracted to obtain a clearer signal on the gas chromatograph. The resulting product gases are then sent to the GC for analysis.

2.2.4 Catalyst Preparation

Appropriate amounts of $Fe(NO_3)_3 \cdot 9H_2O$ (99.99%, Sigma-Aldrich), $Cu(NO_3)_2 \cdot 2.5H_2O$ (98%, Sigma-Aldrich), $Cr(NO_3)_3 \cdot 9H_2O$ (>99.99%, Fisher Scientific) and $La(NO_3)_3 \cdot 6H_2O$ 99.999%, Sigma-Aldrich) were dissolved in de-ionized water and stirred for about 30 minutes. Sodium hydroxide (97.6%, Fisher Scientific) solution was used to increase the pH from acidic (2-3) to basic (pH 11) to form a precipitate.

A calculated amount of sodium hydroxide was added in one quick step to the solution of nitrates to reach a pH of approximately 11. This rapid titration facilitates uniform precipitation of the various metal hydroxide species. Care was taken to avoid pH increases past the desired 11 by a final dropwise titration to the desired pH. Also, the pH meter used measures a local pH, and if stirring is not intense, the signal can be sporadic due to large pH gradients in the thick slurry solution. During and after titration, the solution was stirred by a magnetic stir bar to prevent this problem.

The brown precipitate was vacuum filtered and rinsed at least 3 times with de-ionized water to remove soluble anions and cations. The catalyst was dried in an oven at 60°C overnight and calcined in flowing dry air in a different oven at 300°C for several hours to create the initial oxides.

These catalysts were named as a function of their weight percentage of oxide content (Fe_2O_3, Cr_2O_3, CuO, La_2O_3) expected after this calcination, based on the amounts of nitrates used in their preparation. For example, 83Fe-5La-8Cr-4Cu was prepared to contain 83 wt% Fe_2O_3, 5 wt% La_2O_3, 8 wt% Cr_2O_3 and 4 wt% CuO after calcination in air. After calcination, the catalysts were crushed and sieved to retain particles with sizes between 125-250 μm. Finer particles were pelletized using a 13 mm pellet die in a press, crushed, and sieved again until all catalysts particles were in the desired size range.

2.2.5 Experimental Procedure

The catalyst goes through the following stages in the TPSR experimental design in order to obtain kinetic data from the GC and MS.

1. 0.2 grams of the sieved catalyst particles 150-250 μm are placed into the reactor for 2 hours WGS reduction conditions.
2. WGS conditions continue for 5 days during which GC spectra are taken.
3. Once the reaction has reached equilibrium, a final GC sample is taken and the temperature is changed between 350, 375, 400, and 425°C. The order of the temperatures is randomized. Multiple GC spectra are taken after a half hour at each of these temperatures at varying flowrates. This half hour delay is necessary for the flow rates and temperatures to equilibrate in the system.

A pre-treatment of the catalyst was performed in order to maximize Fe_3O_4 concentration while preventing carbon deposition on the surface of the catalyst. The treatment is done with 12.5 sccm H_2 (AirGas 99.95%), 3.0 sccm CO (Airgas 99.995%), 25 sccm Ar (AirGas 99.997%), and 0.011 mL/min distilled liquid water that passes through a boiler at 300°C. The ratio of mol H_2O/mol CO is 1.2 (R = 1.2). This is done to prevent coking or over-reduction of the catalyst. In a study by Xue et al., a stoichiometric amount of CO and H_2O were added to a blank reactor tube at reaction temperatures, which showed carbon deposition on the quartz tubing (Xue 1996). The study by Xue et al. shows that an R = 1.2 input prevents this coking effect. Coking or carbon deposition could pose a serious problem for UV-Vis analysis in that if a carbon layer is deposited on the catalyst that would significantly change the absorbance of the surface of the catalyst. A series of potential side reactions that can occur under stoichiometric conditions were then hypothesized; these are shown in Table 2.

Table 2 Side reactions at stoichiometric conditions of WGS (Xue 1996)

$$2CO \leftrightarrow C + CO_2$$
$$CO + H_2 \leftrightarrow C + H_2O$$
$$CO_2 + 2H_2 \leftrightarrow C + H_2O$$
$$2CO + 2H_2 \leftrightarrow CO_2 + CH_4$$
$$CO_2 + 4H_2 \leftrightarrow CH_4 + 2H_2O$$
$$C + H_2 \leftrightarrow CH_4$$

Second, WGS conditions were maintained for 5 days while GC samples were taken. WGS conditions are at 400°C, the inlet flows are 20.8 sccm CO and 0.05 mL/min H_2O liquid, and the system was maintained at atmospheric pressure. During this time, the GC peaks were analyzed to show that the reaction had reached steady state. During the initial transient reaction period, the amount of CO_2 produced was higher than at the steady state condition.

Third, once the catalyst reached steady state reaction conditions, i.e. the production of CO_2 stabilized over an extended period of time; two tests were run to determine the initial WGS rates and the activation energies of these catalysts. First, the CO flow rates were changed between 20.8, 41.6, 62.4, and 81.12 sccm at a constant temperature. Secondly the temperatures are changed between 350, 375, 400, and 425°C, and all four flow rates are tested at each temperature. Each flow and temperature condition was held for half an hour before a GC sample was taken to ensure that the reaction reaches steady state conditions at the new flow and temperature. While the catalyst initially took five days to reach equilibrium, much less time was required to equilibrate between small changes in temperature and CO flowrate.

2.3 Results and Discussion

This section discusses the results obtained through the TPSR experimental design as well as the results of the catalyst characterization techniques used.

2.3.1 Catalyst Surface Area and Structural Stability

Structural stability of these catalysts was analyzed through changes in surface area of the catalysts, before and after five days of use under WGS conditions. This was done using BET analysis described in Section 2.1.3. The results for this analysis are shown in Table 3.

Table 3 BET analysis of catalysts before and after reaction

Before Reaction				After Reaction				% decrease			
La%	S.A	Pore Vol	Pore size	La %	S.A	Pore Vol	Pore size	La %	S.A	Pore Vol	Pore size
	(m^2/g)	(cm^3/g)	(Å)		m^2/g	cm^3/g	(Å)		m^2/g	cm^3/g	(Å)
0	8.4			0				0			
1	101	0.101	40.0	1	88.7	0.291	131	1	11.9	-189	-228
2	196	0.199	40.6	2	157	0.342	87.4	2	20.1	-72.0	-115
5	218	0.224	41.0	5	112	0.269	96.3	5	48.6	-20.4	-134
10	196	0.217	44.2	10	111	0.251	90.9	10	43.5	-16.0	-105
20	206	0.230	44.6	20	57.1	0.128	90.1	20	72.2	43.9	-102

This shows that as lanthana is added, there is a significant increase in surface area of the catalyst when compared to the base case 0 wt% lanthana catalyst. The graphical representation of these data is shown in Figure 11. As the percentage of lanthana is increased, the amount of surface area increases, however at higher concentrations of lanthana, the stability decreases. This is seen in the significant increase in the percent of surface area loss before and after reaction of the 20 wt% catalyst compared to the other catalysts. The 1 wt% catalyst decreases 11% in surface area after reaction conditions, while the 20 wt% catalyst loses 72% of its surface area after WGS reaction has taken place.

A possible reason for the increase in the loss of surface area with increasing lanthana is that the increased lanthana is disrupting the previously discussed iron chromium spinel structure.

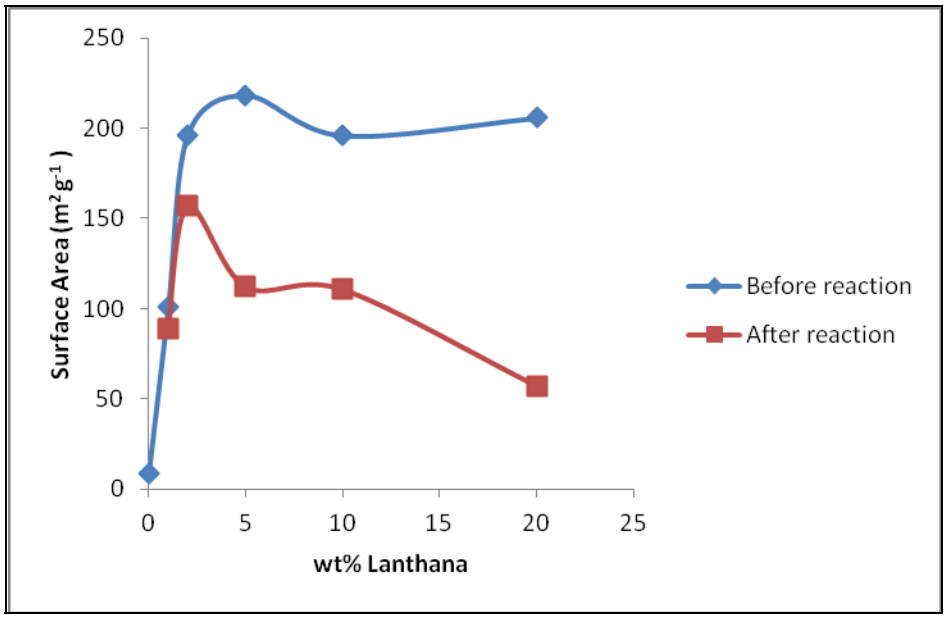

Figure 11 Surface area of catalysts before and after reaction.

There is a significant increase in the amount of surface area measured between the 0 wt% lanthanum catalyst and the 1 and 2 wt% lanthana catalysts. Even a small amount of lanthanum increases the surface area 10 to 20 times more than the base catalyst. This radical change seems to indicate that there is something structurally different with the lanthanum catalyst. XRD analysis will be conducted in future work to confirm the crystal structure difference between the lanthana and base catalysts.

2.3.2 Energy Dispersion X-Ray Spectroscopy (EDX)

Energy Dispersion X-ray Spectroscopy (EDX) is a technique that measures the elemental compositions at points near the catalyst surface to ensure that there is an even distribution of components in the catalyst. This is important in that if all of the lanthana were concentrated in one spot, only a small portion of the catalyst would react differently than the base catalyst. The EDX performed for these catalysts were performed in a line across a surface of catalyst as well

as at individual points. Relative concentrations of the elements are shown in Table 4. The exact weight percentages shown in this table are approximate; however, the EDX does show relatively similar concentrations at a point and across the surface, suggesting that there is an even distribution of particles in the system and that catalyst preparation was done correctly.

Table 4 EDX concentrations of catalysts at a point and across a surface

	One Point Scan					Scan Across Surface				
	La	Cr	Fe	Cu	Total	La	Cr	Fe	Cu	Total
Catalyst ID	(wt%)	(wt%)	(wt%)	(wt%)		(wt%)	(wt%)	(wt%)	(wt%)	
0	0.00	7.86	87.7	4.47	100	0.00	7.93	87.1	4.98	100
1	2.12	7.76	85.9	4.25	100	2.51	7.87	85.2	4.40	100
2	3.08	8.08	84.3	4.54	100	3.46	8.14	84.3	4.12	100
5	6.83	7.84	80.6	4.72	100	7.08	8.50	80.4	4.07	100
10	12.7	7.98	74.8	4.50	100	13.2	8.40	74.1	4.30	100

2.3.3 Rate Analysis

In Section 2.1.2 Experimental Assumptions, the method of initial rates was discussed. In this section the analysis of multiple catalysts utilizing that methodology is discussed. Figure 12 shows the results of varying the flow rates of CO at various temperatures for the 1 wt% lanthana catalyst. Data at multiple flow rates allow for a linear extrapolation back to an infinite flow rate, which represents the initial reaction rate. For example the initial reaction rate at 400°C of the 1 wt% lanthana catalyst is 0.0177 (mol $gcat^{-1}$ min^{-1}). These flow rates are all at the same H_2O to CO ratio of 3:1.

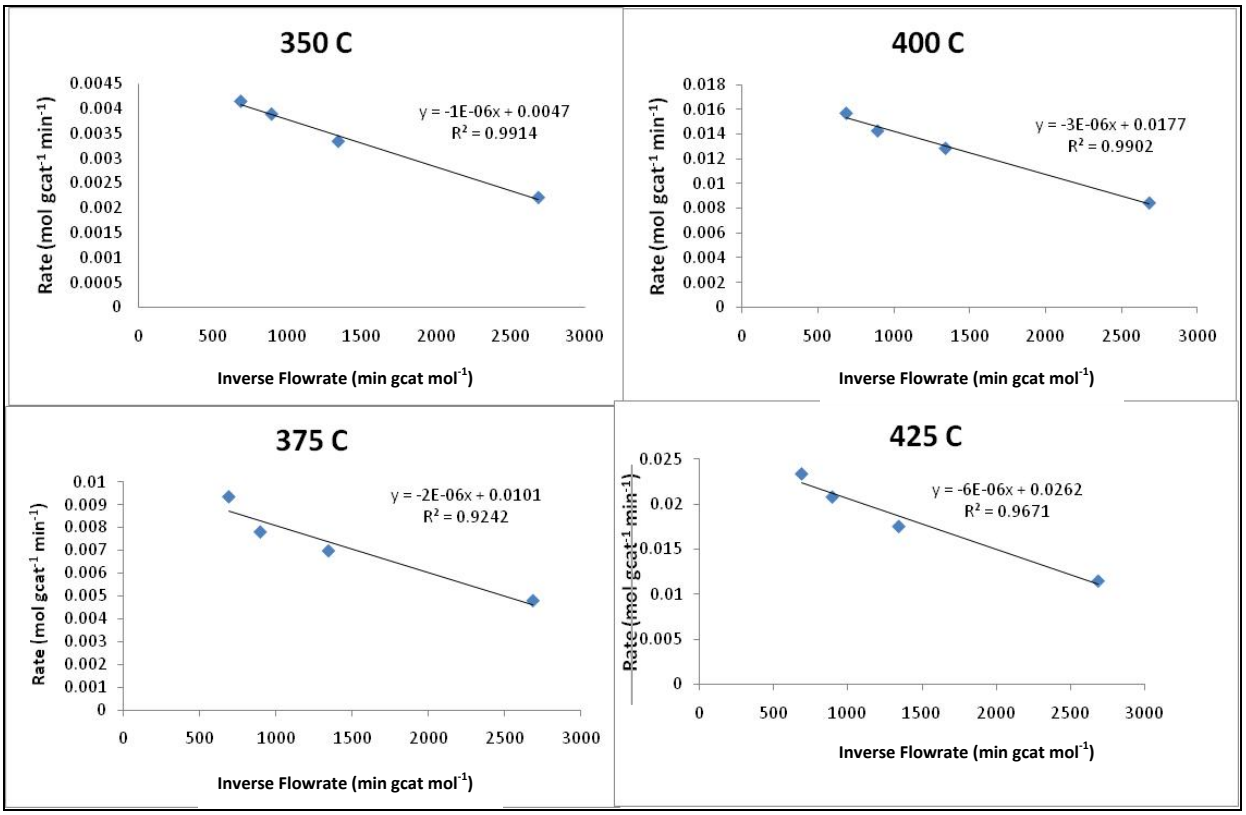

Figure 12 Inverse flow rate versus reaction rate of 1 wt% lanthana catalyst at 4 different temperatures.

2.3.4 Rate Analysis Based on Lanthanum Percentage

The initial rate data compiled from all six catalysts at the various temperatures are shown in Figure 13, which shows that the initial rate data for the 1 wt% lanthana catalyst performed better than any other catalyst at the two extremes of the temperature range, 425°C and 350°C. The 0 wt% catalyst performed best at 375°C and 400°C. This suggests that the lanthana does have a small promotional effect on the WGS reaction as well as a thermal stabilization effect. Also, as the La percentage increases to larger percentages, the activity of the catalyst decreases. This decrease is believed to happen for two reasons: 1) there is less of the active iron phase of

the catalyst with increasing lanthana and 2) the lanthana may disrupt formation of the iron chromia spinel structure discussed in Section 1.6.

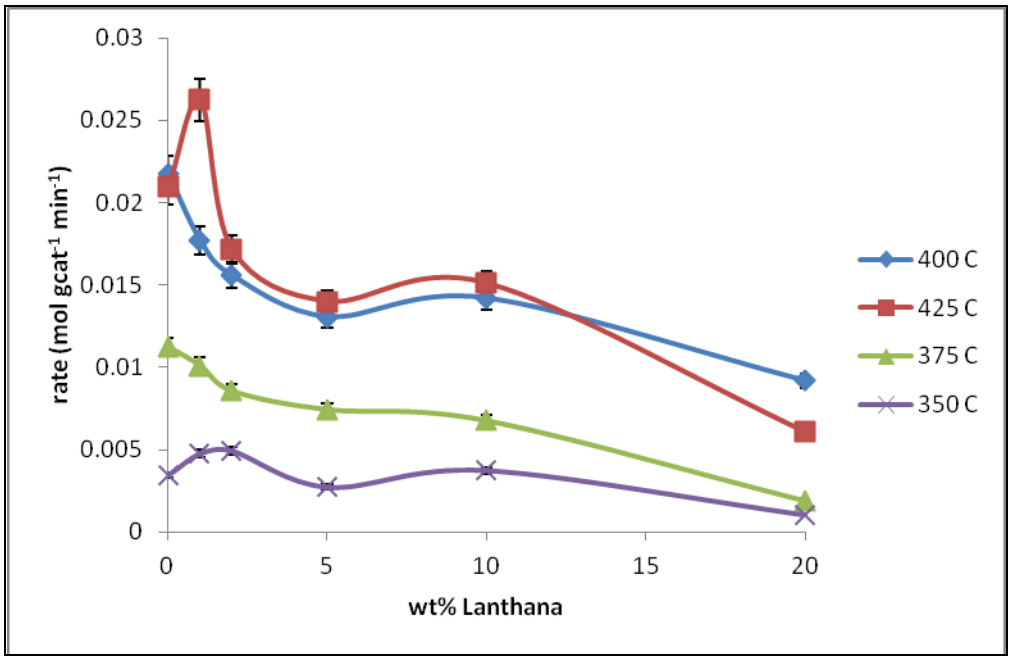

Figure 13 Description of rates as a function of wt% lanthana at various temperatures.

The 20 wt% lanthana catalyst has poor thermal stability, in that the activity of the catalyst decreases as the reaction temperature increases, as explained in section 2.3.5 Rate Analysis Based on Changes in Temperature. The 20 wt% lanthana catalyst also has the least amount of active phase iron in the system because the lanthana is added in place of the iron when these catalysts are made, and thus appears to be at a disadvantage compared to the other catalysts.

There is a slight increase in activity between the 5 wt% lanthana and 10 wt% lanthana catalysts. This suggests that there is some balance between the diminished thermal stability affect, caused by inhibition of the iron-chromia spinel structure, the promotion of the reaction by the La, and the amount of the active Fe_3O_4 phase in the catalyst. The 5 wt% lanthana and 10 wt%

lanthana catalysts have slightly different surface area changes before and after the reaction, with the 5 wt% lanthana catalyst decreasing 48% in surface area and the 10 wt% lanthana catalyst decreasing 43% in surface area. Also, the 10 wt% lanthana catalyst starts with 23 (m^2 g^{-1}) less surface area than the 5% but ends with only 2 (m^2 g^{-1}) less as shown in Table 3, which indicates that the lanthana does provide some stabilizing effect to the catalyst. It appears to be significantly weaker than the iron-chromia spinel structure; however, if the iron-chromia spinel structure is nearly equally inhibited by the lanthana, then the catalyst with the higher lanthana content should be slightly more stable providing more active Fe_3O_4 sites.

2.3.5 Rate Analysis Based on Changes in Temperature

Figure 14 shows how the catalysts performed over a series of temperatures. This figure was created with the same data as Figure 13; however, it shows more clearly the temperature effect of the lanthana. At the lowest temperature tested, 350°C, the 2 wt% lanthana catalyst has a slightly higher initial rate than the 1 wt% lanthana and 0 wt% lanthana catalysts. As temperature increases to 375°C, the reaction rates begin to increase for all the catalysts. The relative increases are fairly similarl for all of the catalysts except for the 20 wt% lanthana, which has a much slower rate increase between 350°C and 375°C, while the 0 wt% lanthana catalyst experiences a sharp increase in rate. The slower rate of the 20 wt% lanthana catalyst could be due to the lack of the iron-chromia spinel structure discussed earlier. The iron chromia spinel provides thermal stability for the catalyst, so a significant decrease in activity with increasing temperature for the highest lanthanum percentage is consistent with this explanation. This concept is shown again in the increase from 375°C to 400°C. The sharp increase in activity for the 0 wt% lanthana catalyst is interesting in that the 1 wt% lanthana catalyst goes through a similar steep ascent between 400°C and 425°C.

Between 375°C to 400°C, the 0 wt% lanthana catalyst still shows the highest rate as well as the highest increase in rate from the previous temperature reading. Finally, the change between 400°C and 425°C shows the 1 wt% lanthana catalyst continuing to increase in activity at even higher rates than the change between 375°C and 400°C.

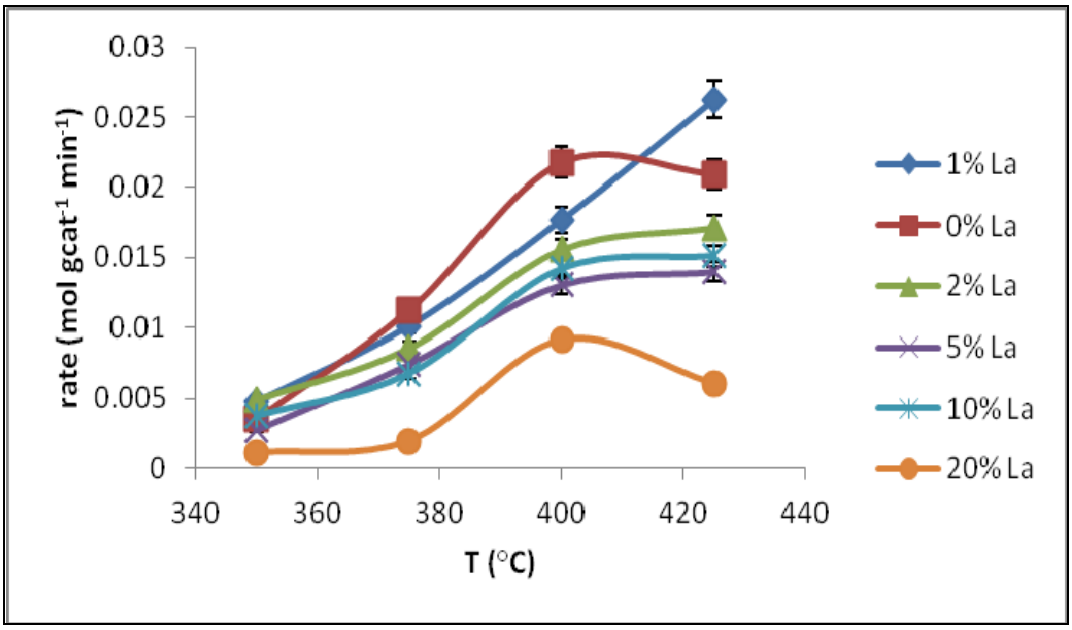

Figure 14 Rates as a function of temperature for all 6 catalysts tested.

This is interesting in that the 0 wt% lanthana catalyst and the 20 wt% lanthana catalyst begin to level off during this transition. The 1 wt% lanthana catalyst has higher activity than the 0 wt% lanthana catalyst at this temperature. This is evidence that concentrations of lanthana that are 1% or lower do not inhibit the chromium's stabilizing effect. Rather, the stabilizing effect of the lanthanum increases the catalyst activity at higher temperatures. This seems to be a cumulative effect of thermal stability from both the spinel structure and the lanthana, as well as the lanthana promotion effect.

2.3.6 Rate Analysis Based on Rate per Surface Area

One of the advantages to rare earth metal oxides, such as lanthana, is the high surface area that it provides to the catalyst, as shown in section 2.3.1 Catalyst Surface Area and Structural Stability. Figure 15 shows the rate in units of (mol m^{-2} min^{-1}). The surface areas of the catalyst change dramatically during reaction so Figure 15 shows the initial rates based on both the initial surface area and the post-reaction conditions surface area. This form of the rate data shows the superiority of the 1 wt% lanthana catalyst compared to the other lanthanum catalysts.

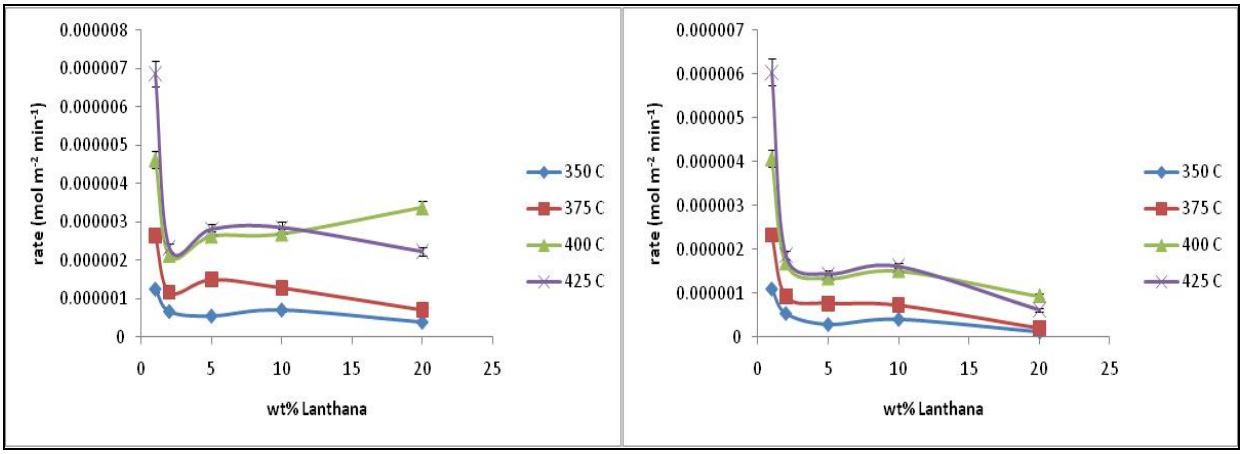

Figure 15 Rate as a function of surface area for the lanthanum catalysts. Per surface area of the catalyst after the reaction on the left and per surface area of the catalyst before reaction shown on the right.

The reaction rate using the 1 wt% lanthana is 30-48% higher than the next closest catalyst. The rate per surface area of the 0 wt% lanthana catalyst is not shown here, due to the base catalyst having significantly lower starting and ending surface areas than the lanthana catalysts which significantly skews the data. Similarly the 20 wt% lanthana catalyst has a higher rate/SA after reaction when compared to before reaction due to the 78% reduction in surface

area, which shows that despite the loss of surface area, the remaining area possesses similar activity compared to the other catalysts with higher lanthana contents.

2.4 Conclusions

The addition of 1 wt% lanthana to the Fe-Cr-Cu catalysts increases reaction rates of the catalyst at 425°C and 350°C, however the 0 wt% lanthana catalyst has the highest rates at 375°C and 400°C. The 0 wt% lanthana catalyst shows significant drop off in rate at the 425°C mark, suggesting that the lanthana provides a thermal stabilizing effect at higher temperatures. This effect is smaller than the iron-chromia spinel effect; however, small doses of lanthana have a compound thermal stabilizing effect. The increased reaction rates at higher temperatures could allow for greater throughput of reactants in industrial settings.

Higher concentrations of lanthana decrease the activity due to what is believed to be inhibition of the iron-chromia spinel structure as well as reduced amount of the active phase of catalyst. The lanthana addition to the catalysts greatly increases the surface area of the WGS catalysts (~40 (m^2 g^{-1}) to upwards of 200 (m^2 g^{-1})). This surface area increase however did not seem to have a great effect on the overall activity of these catalysts. Lanthana also lowers the activity of the catalysts in higher concentrations.

As discussed in Section 2.3.2, the catalysts were also characterized using EDX and showed an even distribution of components throughout the system, suggesting that the co-precipitation method of making these catalysts leads to a solid solution of components.

Chapter 3 UV-Visible Assessment

3.1 Introduction

This chapter will discuss the UV-Visible spectroscopic methods and results.

3.1.1 UV-Visible Spectrometer (In-situ)

Figure 16 shows the Varian Cary 4000 UV-visible spectrometer used during this study. A reactor with optically clear quartz windows contains catalyst in the sampling bay where it is exposed to light. The reflected light is measured to quantify the changes in intensity of only the diffusely reflected light from the catalyst surface, which is normalized relative to the reference light intensity via the Kubelka-Munk equation described in Section 3.1.6.

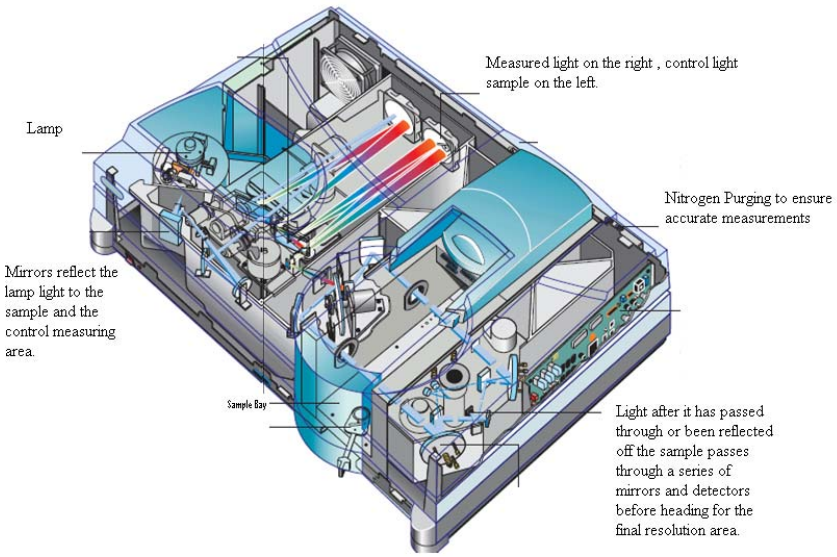

Figure 16 Varian Cary 4000 UV-vis spectrometer provided by Varian Corporation (Varian Corp 2010).

3.1.2 UV-Visible Spectroscopy

One method of UV visible spectroscopy involves exposing a catalyst sample to a broad spectrum of UV and visible wavelengths and detecting the absorbed portions of the diffusely reflected light as a function of wavelength based on electron states of the samples. Using MoO_x species, Che's group showed that the number of Mo species in an oxide cluster could be determined. From that work, Webster determined the edge energy of a cluster and correlated that to the number of bridging Mo-O-Mo bonds. In addition, UV–vis can also monitor the extent of reduction of fully oxidized cations due to ligand to metal charge transfer (LMCT) transitions (Wachs 2005). UV-visible spectra can gather information on the Fermi energy bands of metal and metal oxide catalysts via the reflection of light from the catalyst surface. This information can lead to new insights of molecular configurations on the surface as well as oxidation states of the catalytic material.

3.1.3 Extent of Reduction

Extent of reduction refers to the relative oxidation state of a material compared to a "fully oxidized" baseline condition. For example, in the WGS reaction, the iron may undergo transitions from Fe_2O_3 to Fe_3O_4 to FeO to Fe metal. The oxidation states of the iron are respectively 3^+, 2.7^+, 2^+, and 0 in metallic iron. Being able to determine how much of each of these components is present at any given time is useful in that the Fe_3O_4 is the active phase in the WGS reaction. A simple average of the oxidation states is not sufficient because only the Fe_3O_4 is desired for the forward reaction.

3.1.4 X-Ray Adsorption Near Edge Spectrocopy (XANES)

XANES is a means by which a synchrotron is used to determine extent of reduction of a catalyst. While a XANES study will not be performed in this work, XANES is a well understood

method for obtaining the extent of reduction data that this study is trying to find utilizing UV-visible spectroscopy. Therefore, a brief introduction to spectroscopic methods of determining extent of reduction is outlined in the following sections.

The synchrotron radiation required to perform a XANES spectra can provide an intense source of radiation over a very wide range of energies. The intensity of synchrotron radiation is thousands to millions of times greater than that of more common laboratory X-ray sources over this wide energy range, greatly increasing the sensitivity of this type of spectroscopy (Gunter 2002).

Figure 17 depicts various XANES spectra of a mineral, mantle garnet, in which different extent of reductions are being tested. The difference between the 10 spectra in Figure 17 is the concentration of the Fe^{3+} oxidation state, with spectra "j" being pure Fe^{3+} and spectra "a" being 9% Fe^{3+}. An unknown sample of garnet could now be compared to these normalized scans to determine the Fe^{3+} quantity. The "and", "alm", and "ski", in the figure represent three different types of iron garnet configurations: andradite, almandine, and skiagite. While these iron compounds are not used in WGS reaction, the concept that various forms of iron can be distinguished via this spectroscopic technique serves as the basis for the eventual goal of this project; to use UV-vis spectra to determine the overall extent of reduction of the system under WGS conditions.

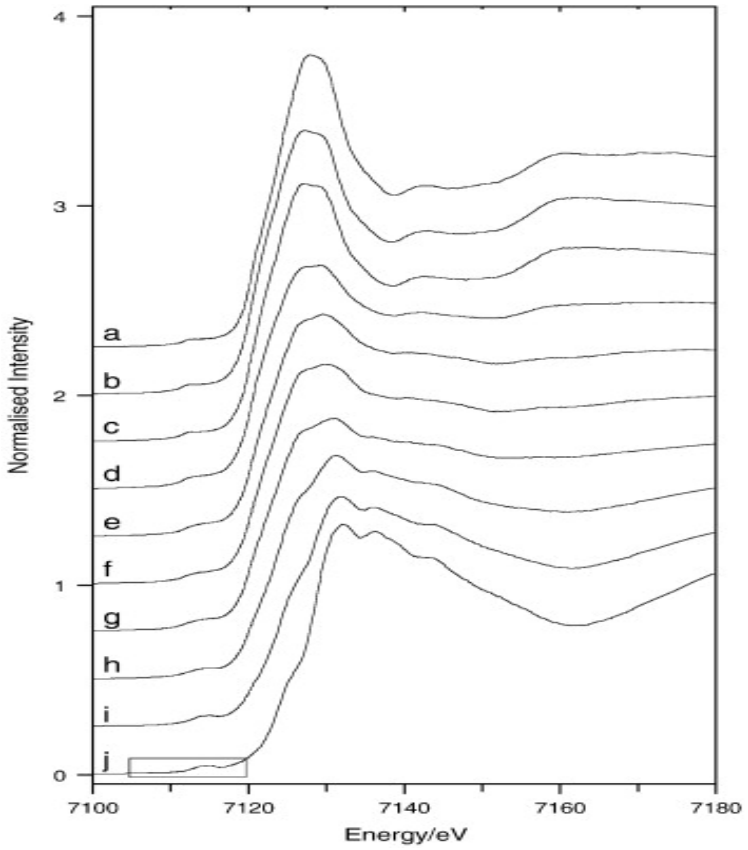

Figure 17 Normalized Fe K-edge XANES spectra of (a) mantle garnet ($Fe^{3+}/\Sigma Fe = 0.090$, Mon F), (b) alm0.93ski0.07 ($Fe^{3+}/\Sigma Fe = 0.045$), (c) alm0.79ski0.21 ($Fe^{3+}/\Sigma Fe = 0.123$), (d) alm0.51ski0.49 ($Fe^{3+}/\Sigma Fe = 0.246$), (e) alm0.12ski0.88 ($Fe^{3+}/\Sigma Fe = 0.370$), (f) and0.21ski0.79 ($Fe^{3+}/\Sigma Fe = 0.458$), (g) and0.45ski0.55 ($Fe^{3+}/\Sigma Fe = 0.548$), (h) and0.72ski0.28 ($Fe^{3+}/\Sigma Fe = 0.704$), (i) and0.93ski0.07 ($Fe^{3+}/\Sigma Fe = 0.905$), and (j) and1.0 ($Fe^{3+}/\Sigma Fe = 1.000$). The spectra have been offset for clarity (Berry 2010).

3.1.5 Edge and Pre-Edge Energies

Figure 18 shows the XANES spectra of iron. While the data in Figure 17 were normalized for clarity in interpretation, Figure 18 has not been normalized. The two energies that are important to note are the edge and pre-edge energies. As samples of varying oxidation states are taken, the pre edge energies will be distinctly different, while the edge energies are nearly identical for all the iron oxidation states. The X-ray energy absorbed during XANES causes an

electron in a lower orbital to move to a higher unoccupied orbital. The effect of decreasing shielding as the oxidation state increases is to lower the energy of all of the bound orbitals, such as 1s, and to increase the energy spacing between the 1s and the continuum. This is what causes the increase in the energy of the absorption edge with increasing oxidation state. Thus, the absorption edge positions of different complexes of the same oxidation state are similar (Gunter 2002).

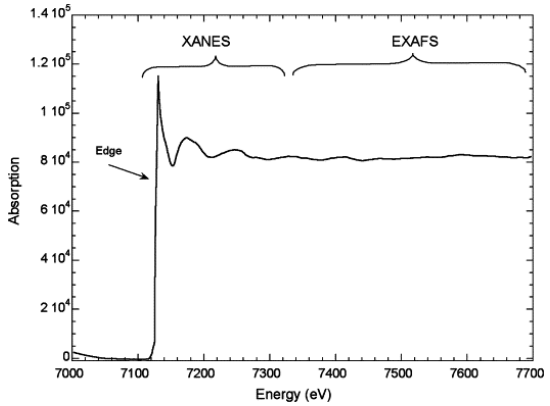

Figure 18 The extended x-ray absorption fine structure (EXAFS) and XANES absorption spectrum of iron. This shows the edge, the XANES region, and the EXAFS region. This spectrum has not been corrected for background, nor divided by current (Gunter 2002).

Therefore, as different samples with differing extents of reduction approach the edge energy, the spectra begin to align on top of each other. Thus the pre-edge energy spectra contain the most useful information in determining extent of reduction of a given sample.

3.1.6 Kubelka-Munk Function

The XANES system described above creates spectra of relative intensity versus energy, to determine extent of reduction. To obtain extent of reduction utilizing UV-visible spectroscopy, similar relative intensity versus energy spectra must be produced.

The Kubelka-Munk model for diffuse reflectance involves balancing two differential equations for the flux of light (I) into and through a surface and flux reflected from within and away from that surface (J). These two differential equations are

$$dI/dx = -(k' + s)I + sJ \quad (5)$$

$$dJ/dx = (k' + s)J - sI \quad (6)$$

where k is the absorption coefficient and s is the scattering coefficient. The balance of these two fluxes is expressed in terms of a normalized reflectance, R_∞, which is the ratio of the reflectance of the sample to a reference reflectance, ideally based on a perfect reflector, but in practice a white substance, such as magnesium oxide (MgO) or Teflon, is used as the reference. The solution to the coupled differential equations then simplifies to the following equation, called the Kubelka-Munk function (Christy 1995):

$$F(R_\infty) = (1 - R_\infty)^2(2R_\infty)^{-1} = K(S)^{-1} \quad (7)$$

where K and S are proportional to the absorption and scattering coefficients, respectively. In a diffuse reflectance spectrum, the ratio of the light scattered from an infinitely thick layer and the scattered light from an ideal non-absorbing reference sample is measured as a function of the wavelength, λ (Weckhuysen 1999).

Similar to the Weckhuysen's study of a pure metal oxide on an irreducible support, correlation of the diffuse reflectance spectra obtained for fully oxidized mixed-oxide catalysts with those for the same catalysts reduced with quantified amounts of hydrogen during TPR's is hypothesized to determine the extent of reduction of unknown samples using UV-visible spectroscopy.

3.1.7 Extent of Reduction via UV-Visible Analysis

In an extended solid, different oxidation states of an element have different Fermi energy levels. These differences are detectable by absorption or reflection of different intensities of UV-visible light. In a study by Weckhuysen, in-situ UV-vis spectra were recorded for Cr^{+6} and Cr^{+3} oxidation states. Initially, nearly the entire sample was Cr^{+6}; as time progressed, the energy peak that corresponds to the pure Cr^{+6} lowered in intensity as more Cr^{+3} was produced from the reduction of Cr^{+6}. Figure 19 contains the results of the in-situ analysis for these catalysts, with the arrow showing the measurements taken in time from start to finish. As the peak near 400 nm decreases, the peak near 650 nm increases. This variation from the Cr^{+6} pure oxidized state measures the extent of reduction of that catalyst as a function of time (Weckhuysen 2000).

Similarly, this study will use the UV-Visible technique used by Weckhuysen to measure the changes in the iron oxidation state from the Fe^{3+} state to various lower oxidation states. As the iron changes oxidation states the normalized absorbance of the surface, or Kubelka Munk value, will increase. This leads to a direct correlation between the absorbance of the sample and extent of reduction of the catalyst.

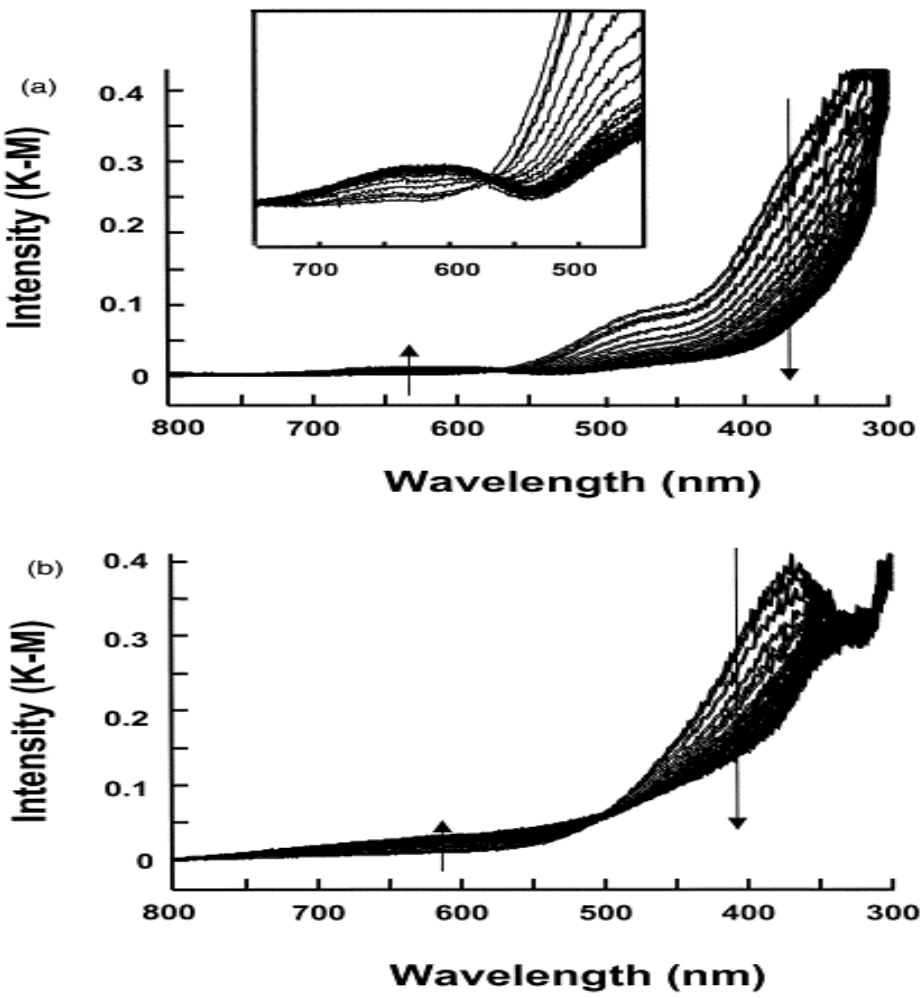

Figure 19 (A) In situ UV–Vis diffuse reflectance spectra of 0.5 wt.% CrO_x/SiO_2 catalyst treated at 350°C in 2% isobutane in N_2 as a function of time. (B) In situ UV–vis diffuse reflectance spectra of 0.5 wt.% CrO_x/Al_2O_3 catalyst treated at 350°C in 2% isobutane in N_2 as a function of time (Weckhuysen 2000).

3.1.8 Structural Stability in the UV-Visible In-situ Reactor

During initial experiments, the sample cup was filled with a 1:1 mixture of quartz chips to catalyst with 180-250 micron particles. A thermocouple installed in the Praying Mantis cell and inserted into the top of the cup at an angle that does not inhibit the collection of diffuse

reflectance spectra from the center of the catalyst sampling surface was used to measure the catalyst temperature.

Quartz chips were added to the system to prevent agglomeration of catalyst particles under WGS conditions. In preliminary experiments, the catalyst particles agglomerated when water was added to the system and then expanded, forming a dome on top of the sample cup. With the catalyst no longer forming a flat surface to reflect the light, no meaningful UV-Visible spectra could be obtained. Quartz chip dilution did not help the catalyst agglomeration problem.

To address this agglomeration problem, a catalyst pellet was used. The pellet was made at 5000 psi of compression and placed on top of a quartz particle bed. Figure 20 shows a photograph of the pelletized catalyst in the Harrick cell. The bottom and sides of the pellet chipped off into small particles that then agglomerated, and expanded, clogging the flow of the inlet gases causing the inlet gases to build up pressure. Then, the pressure released, causing the pellet to flip out of the sample cup.

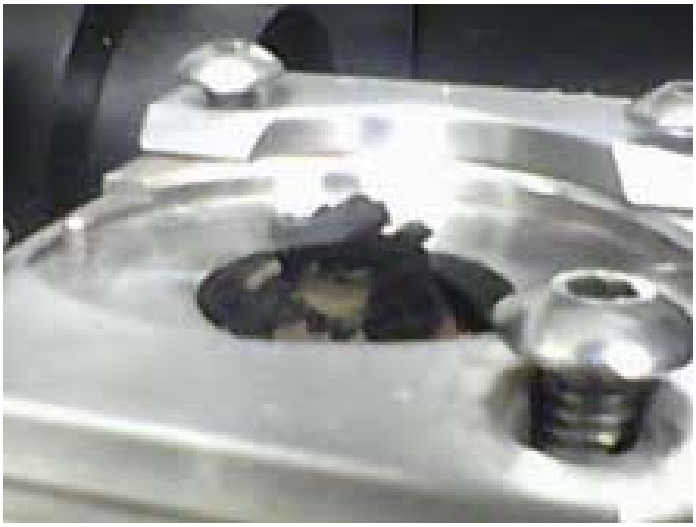

Figure 20 Pellet catalyst under WGS conditions.

With the powdered catalyst, the agglomeration took a few hours. With the pellet, a full 30 hours of usable surface conditions were maintained. The initial surface of the pellet is still smooth; meaning that had the pressure build up not occurred, data could have been gathered indefinitely. Neither the TPR nor TPO requires the addition of water. The results of the collected TPR and TPO data will be discussed in an upcoming section.

Section 1.7 discussed the formation of the iron-chromia spinel structure. The iron-chromia spinel is supposed to inhibit this type of rapid sintering and agglomeration, providing stability to the WGS catalyst. This spinel structure is normally formed via pre-treatment; however, for these catalysts the spinel structure was formed in-situ with the UV-Vis system. The formation of the spinel structure itself, could cause a small volumetric expansion that could account for this type of morphological response, however this post WGS conditions structural study will be performed as future work.

3.1.9 Reversibility of the Absorbance Spectra of the Catalysts

The topic of reversibility of the absorbance spectra of each catalyst being analyzed will be discussed in upcoming sections. If a catalyst's absorbance spectrum is fully reversible between repeated reductions and oxidations, then the absorbance spectra should line up exactly on top of each other. The data will show that this is not the case, which is not unexpected due to the morphological changes suggested by the decrease in surface area of the catalysts discussed previously. Reversibility is not important to the activity of the catalyst in WGS reaction conditions, however it will facilitate future analysis of the extent of reduction calculation utilizing UV-visible spectroscopy.

3.2 Experimental Methods

This section outlines the equipment and methodology used in order to obtain UV-Visible spectra of the catalysts.

3.2.1 UV-Visible Diffuse Reflectance Apparatus

As shown above in Figure 7, the experimental apparatus utilizes multiple 3-way valves to allow all of the aforementioned reactant gases to go to both the TPSR and the UV-Visible spectrophotometer (UV-Vis). Water is added via a bubbler into the system, instead of the syringe pump and boiler, like in the TPSR experiment because the UV-Vis (as explained in Section 3.1) contains a HARRICK Praying Mantis Cell that cannot be heat traced. Therefore, there is a cold spot in the line that would condense water, which would fog the quartz windows of the cell and create pressure spikes as the condensed water reaches a heated section of the line and boils in the system. The partial pressure of water was assumed to be equal to the saturation pressure at ambient conditions. This assumption is reasonable for the small bubbles formed in the bubbler, since the flow rates of the inlet gases are low (50 sccm), which allows sufficient time for saturation. Air is added into the system using an Omega® direct read 100 sccm rotameter calibrated for airflow.

The combined gases are then sent into the HARRICK Praying Mantis cell from beneath the sample cup. This allows the gases to preheat before reaching the catalyst surface, as opposed to being heated at the surface. Coming from underneath however does limit the flow rate of the inlet gases in that too high of an inlet flow will disrupt the smooth sampling surface of the catalyst for the UV-visible experiments.

Following the UV-Vis reactor, the product gases were routed to an MKS Cirrus 100 mass spectrometer (MS). As described previously, the MS detects concentration changes of product gases with time to quantify the temporal evolution of the reactants and products. This acts as a check of kinetic data with the TPSR design as well as allows for inferences of extent of reduction of the catalyst.

3.2.2 Diffuse Reflectance Spectroscopy Using a Harrick Praying Mantis Cell

Diffuse reflectance spectroscopy involves the illumination of powdered samples by incident radiation. The incident light is partially absorbed, partially scattered. The scattered radiation, emanating from the sample is collected in an integration sphere and detected. The figure below shows a schematic overview of diffuse reflectance spectroscopy.

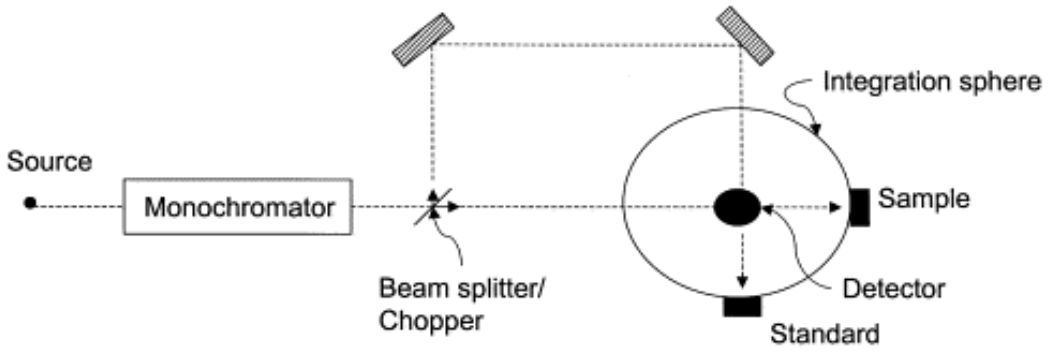

Figure 21 Schematic overview of a diffuse reflectance spectrophotometer with integration sphere (Weckhuysen 1999).

The ideal integration sphere, or area in which the differential radiation equation (which simplifies to the Kubelka-Munk equation) is solved, is approximated by the Harrick Praying Mantis Cell shown in Figure 22. This cell sits in the sample bay of the Varian Cary 4000 UV-visble spectrometer shown in Figure 21. The cell focuses the incident light on the catalyst, which

sits in a small sample cup inside the mantis cell. The reflected light is captured by a series of mirrors and routed to the detector.

The purpose of this cell and reaction chamber is to minimize the specular reflection of the light off of the surface. Specular reflection is the direct reflection of light in a single direction at the exact angle of incidence, like a mirror. This type of reflectance will create large spikes in signal that will overshadow the diffuse reflectance data. Figure 22 shows the arrangement of the mirrors and the light path within the praying mantis cell.

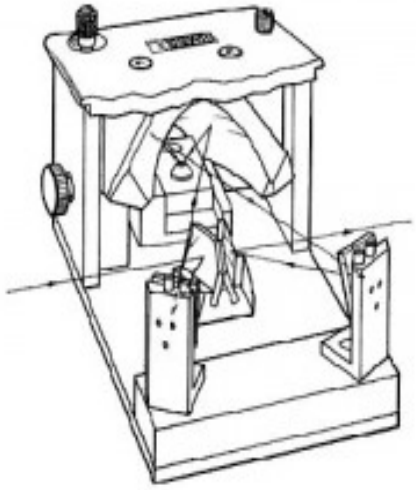

Figure 22 Harrick Praying Mantis Cell (Harrick Scientific 2012).

3.2.3 Challenges and Previous Measurements

UV-visible spectroscopy requires that the light that hits the catalyst surface be reflected back from the surface to measure a change in intensity. Previous UV-Vis measurements of high loading iron catalysts, like the WGS catalyst, have not been previously done. However, previous diffuse reflectance UV-visible spectra of iron samples have been taken with low amounts of iron (3-5 wt%) (Herranz 2006). The results are shown in Figure 23.

These spectra show not only the iron content of the catalyst, but also that variations in preparation of the catalyst can result in significant differences in the UV-visible spectra. Therefore, the first major challenge in obtaining reliable results for these spectra analyses are repeatable catalyst preparation (Herranz 2006).

The second major challenge with using the in-situ UV-vis spectroscopy is that high temperature WGS reaction iron catalysts are visibly black. Black objects absorb visible light and if no light is reflected from the surface of the catalyst, then no data can be gathered. Previously, this problem was solved by using low concentrations of iron, giving the catalyst a rust red color.

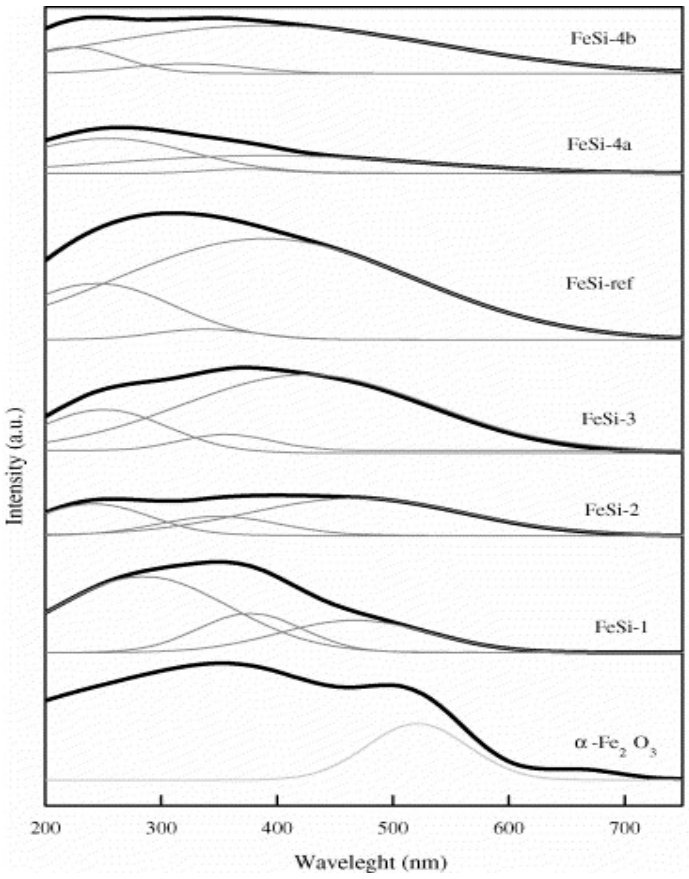

Figure 23. UV vis spectra for different iron based catalysts. The light gray lines represent calculated deconvolutions of the apparent constituent peaks that make up the actual spectra, which is the black, bold line (Herranz 2006).

This experiment extracted data from the 70-90 wt% FeO_x catalyst compositions used in industry. The hypothesis was that while these catalysts are black in the visible region, they may provide useful data in the UV region or there may be bands in the visible region that produce a usable signal. UV-vis spectroscopy has the potential to inexpensively and efficiently measure the extent of reduction of these catalysts in-situ to provide new insight into the WGS mechanism that would normally only be available through more complicated experiments, such as X-ray absorption spectroscopy.

3.2.4 Data Gathering Procedure for the UV-Visible In-situ Reactor

Each catalyst that was examined in the UV-vis spectrometer was subjected to the same series of seven reaction steps:

1. Initial oxidation and baseline scan
2. Temperature Programmed Reduction 1 (TPR1)
3. Temperature Programmed Oxidation 1 (TPO1)
4. TPR2
5. TPO2
6. Water Gas Shift Pre-Treatment
7. Water Gas Shift Conditions

After the initial catalyst preparation and calcination, the catalyst has potentially a mixture of Fe_3O_4 and Fe_2O_3. The initial oxidation step is a flow of 30 sccm of AirGas® Ultra Zero Air (79% N_2 21% O_2) at 400 °C for at least a half hour. A baseline absorbance scan is then taken from 12,500 wavenumbers to 50,000 wavenumbers (or cm^{-1}) via Varian® Scan program. This fully

oxidized baseline serves as the comparison sample, instead of MgO, for the Kubelka Munk function for all future scans.

The catalyst is then cooled at a rate of 10°C/min back to room temperature to avoid thermal shock, at which point the air flow is shut off and a mixture of 47.5 sccm Ar (AirGas 99.997%) and 2.5 sccm H_2 (AirGas 99.95%) is introduced. After a half hour of exposure at room temperature for the system to equilibrate, the temperature is increased at 10°C/min up to 400°C. This will also allow inference of initial oxidation states and optimum extents of reduction in the catalysts. During this time, both the Varian Kinetics software as well as the MKS Cirrus Mass Spectrometer collect data. The amount of hydrogen that leaves the system was then subtracted from the amount entering the system, as determined from the mass spectrometer. The consumption rate of hydrogen is then equal to the rate of reduction of the catalyst.

The Varian Kinetics Program collects absorbance as a function of time at a specific wavelength. This study utilizes 800 nanometers or 12,500 wavenumbers. The MS measures concentrations of the various components as a function of time. The programs are run for 3 hours to assure that an accurate baseline concentration for the MS can be obtained. After 3 h, the catalyst is then analyzed utilizing the Kubelka Munk function on the Varian Scan program; which compares the catalysts absorption after the TPR to the initial oxidation baseline across the 12,500-50,000 wavenumber range of frequencies.

The catalyst is then cooled in preparation for step three, TPO1, in which 30 sccm of air flow into the system with a steady ramp increase of 10°C/min for the same total time and utilizing the same computer programs discussed in the TPR1 step. Afterwards, a Kubelka Munk scan is also taken to compare the initial baseline to the re-oxidized catalyst. If the catalyst

reaction were reversible, the reduction and re-oxidation of the catalyst would have no effect on the activity and absorption of the catalyst and the Kubelka Munk scan should read zero across all frequencies, since it is referenced to the initial fully oxidized catalyst.

The catalyst is then cooled and goes through a similar procedure as TPR1 to measure the stability and reversibility of the catalyst. Ideally, the scan at the end of TPR2 should line up directly on top of the scan for TPR1. This would indicate that there is no decrease in the activity of the catalyst through multiple cycles of oxidation and reduction.

The catalyst is then cooled again and goes through a second TPO similar to the first, with the exception that the catalyst is not cooled down after this step. The catalyst is then ready to begin water gas shift reduction conditions.

WGS pre-treatment conditions involve a mixture of 12.5 sccm H_2, 3 sccm CO (Airgas 99.995%), 25 sccm Ar, flowing through a distilled water bubbler for 2 hours. This mixture of inlet gases is used to maximize the amount of Fe_3O_4, the active iron phase, in the catalyst. During this process the mass spectrometer gathers concentration data to show production of hydrogen near the completed stages of the reduction process.

After the WGS reduction, the hydrogen flow is turned off, while the WGS conditions proceed as long as possible, ideally ~100 h. Challenges in collecting the WGS data were explained in section 3.1.8 Structural Stability in the UV-Visible In-situ Reactor. UV-visible scans were taken across the frequency spectrum at regular intervals to show changes in the oxidation states of the surface.

3.2.5 Methodology of UV-Visible Software

The Varian Scan® program scans over a series of frequencies, 12,500 to 50,000 cm^{-1}, and measures the absorbance at each frequency. Traditionally, the catalysts are measured against a white catalyst, something that will reflect the vast majority of the light in order to have a comparison point to absorption spectra from the sample. In this study, the fully oxidized catalyst was used as a baseline for all Kubelka Munk calculations (the Kubelka Munk equations were discussed in detail in Section 3.1.6 Kubelka-Munk Function). This is done by placing fresh catalyst in the system and flowing air (Air Gas Ultra Zero air 20% O_2) over the catalyst for 30 minutes at 400°C. This fully oxidized baseline acts as a better comparison for the Kubelka Munk function for these catalysts because the catalyst is mostly black because it provides greater sensitivity compared to the conventional white reference sample.

The UV-Visible spectrometer runs simultaneously with the mass spectrometer. The time axis on the Kinetics® program line up exactly with the time and temperature scales in Figure 24 TPR 1 of 1wt% lanthana catalyst data from mass spectrometer. The Kinetics® program measures the catalyst absorbance at a set frequency, 12,500 cm^{-1} or 800 nm for these experiments. This frequency is used because it shows the greatest change in absorbance during reaction conditions.

3.3 Results and Discussion

This section discusses the results obtained through the UV-Vis experimental design.

3.3.1 TPR and TPO Results and Discussion

As previously described, both the TPR's and TPO's require mass spectrometer and UV-Visible data. This section will discuss both sets of data and how they relate to each other.

3.3.2 TPR and TPO Analysis via Mass Spectrometer

Figure 24 TPR 1 of 1wt% lanthana catalyst data from mass spectrometer shows the output from the initial TPR of the 1 wt% lanthana catalyst. The red line represents hydrogen consumption, while the green line is water production. The red line dips as the green line increases. This shows the reduction taking place, i.e.

$$3Fe_2O_3 + H_2 \leftrightarrow 2Fe_3O_4 + H_2O \qquad (8)$$

The two peaks are slightly offset from each other, which is due to differences between the gas molecules. Water is much more polar than hydrogen and more likely to adsorb to the surfaces inside in the MS chamber, making them have a longer residence time in the chamber than the hydrogen. This is also the reason for the water having a much broader peak than the hydrogen and a seemingly larger area. For these reasons, determinations of reaction rates were calculated using the hydrogen consumption line.

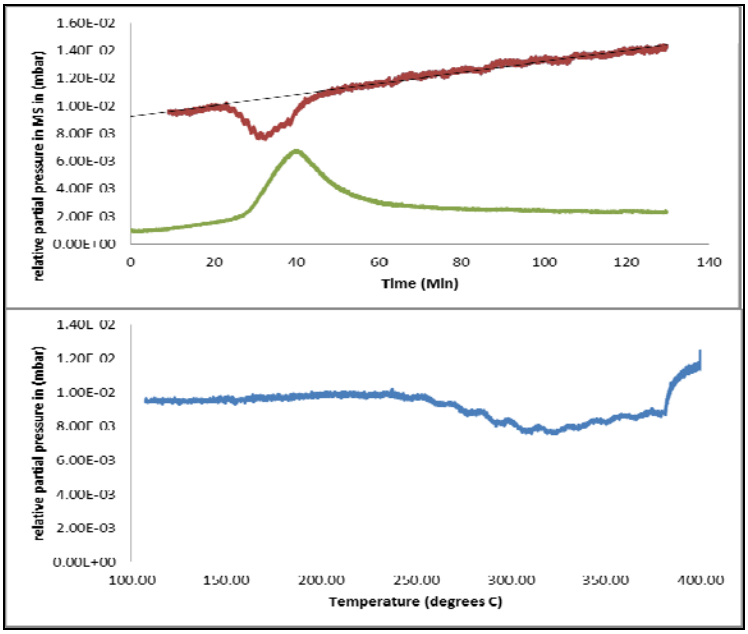

Figure 24 TPR 1 of 1wt% lanthana catalyst data from mass spectrometer.

The best fit line is assumed to be the inlet baseline concentration of hydrogen. The baseline for the hydrogen can change from run to run as explained in section 2.2.2 Mass Spectrometer. Therefore the fit line shown above represents the inlet flow rate of 2.5 sccm hydrogen. Numerically integrating the area below the data line and subtracting it from the area below the fit line results in the area of consumption of the hydrogen. The percentage of the inlet hydrogen consumed is then calculated. Using the inlet flow rate, the total number of moles of hydrogen consumed was calculated. Similar measurements and calculations for the TPO's were performed to measure the amount of oxygen consumed. Table 6 shows the moles of hydrogen or oxygen consumed for each catalyst tested, the amount of time over which consumption took place and the peak temperature of consumption.

Table 5 Summary of hydrogen and oxygen consumption via mass spectrometry

Catalyst ID	Percentage of inlet consumed	Moles consumed	Time of Consumption (min)	R squared of linear fit line	Peak Temp (°C)
TPR1 1La	1.14E-01	2.97E-04	29	9.83E-01	306
TPR2 1La	5.44E-02	1.65E-04	34	9.15E-01	364
TPO1 1La	2.97E-02	2.61E-04	40	9.88E-01	365
TPR1 5La	8.94E-02	1.38E-04	17	9.62E-01	286
TPR2 5La	5.30E-02	2.42E-04	50	9.98E-02	298
TPO1 5La	1.90E-02	1.22E-04	30	9.98E-01	324
TPR1 10La	6.74E-02	2.23E-04	37	9.60E-01	315
TPR2 10La	3.49E-02	9.37E-05	30	9.30E-01	338
TPO1 10La	3.54E-02	2.66E-04	35	9.90E-01	255

From these data, the 1 wt% lanthana catalyst consumed the most hydrogen; 2.97×10^{-4} mol. Figure 25 shows the graphic comparison of each of the catalysts for their respective runs. In all cases, TPR2 consumes less than TPR1, which shows that the TPR/TPO process is not fully reversible because the two lines are not identical. The time of consumption for each of the catalysts increases from TPR1 to TPR2. Suggesting that there is some added limiting effect

caused by the reduction-oxidation-reduction cycle. The number of moles consumed decreases significantly as shown in Figure 26.

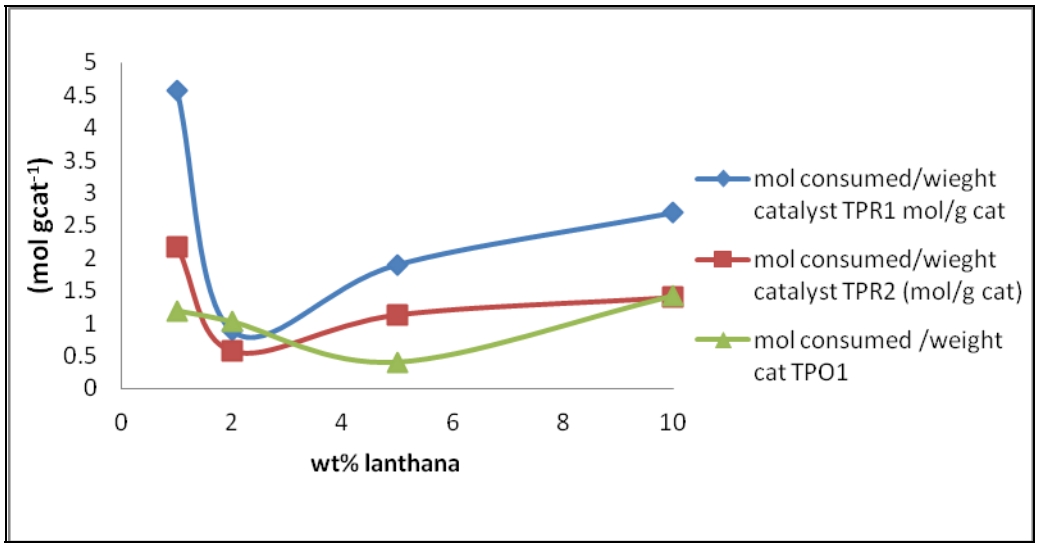

Figure 25 TPR/TPO consumption per gram catalyst.

Also, the temperature of greatest consumption increases from TPR1 to TPR2. The blue line in Figure 24 shows the hydrogen profile with respect to temperature. The greatest deviation from the baseline of the hydrogen is considered to be the peak temperature of consumption of hydrogen. Figure 25 shows that with increasing lanthana, there is a decrease in the moles of H_2 consumed. This suggests that the 1 wt% lanthana catalyst is more reducible than the other catalysts.

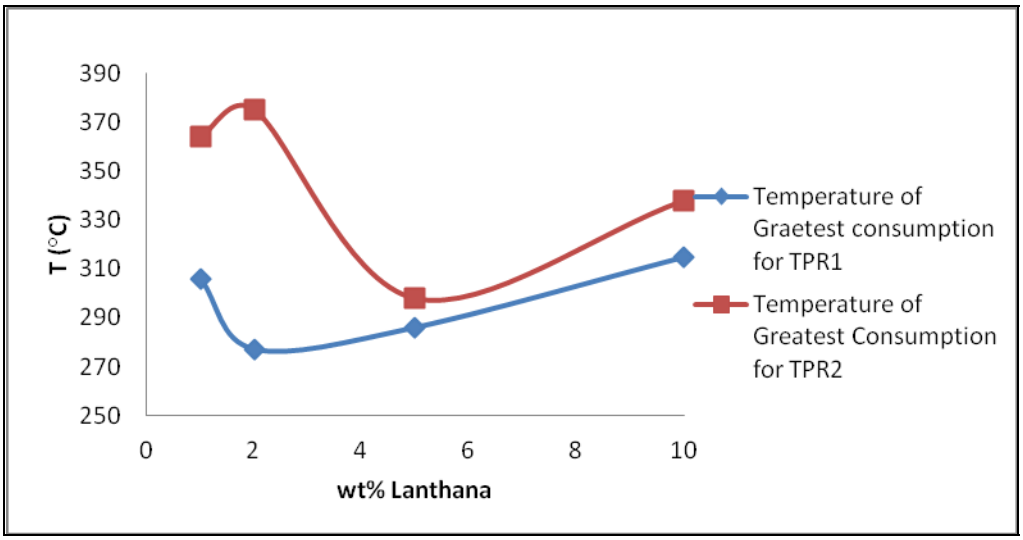

Figure 26 Change in peak temperature for TPR1 and TPR2.

The moles of oxygen consumed also increases slightly as the lanthana content of the catalysts increases. This could be due to the lanthana increasing the oxidation activity of the catalysts by adsorbing more oxygen, but it is more likely that the lanthana is facilitating the oxygen desorption step like cerium does as explained in Section 1.4. However, as the lanthana content is increased, the difference between TPR1 and TPR2 decreases for each of the catalysts.

3.3.3 TPR and TPO Analysis via UV-Visible Kinetics® Program

The data are represented first by time and second by temperature. The first graph shows how the absorbance changes as the redox reaction process (TPR1→TPO1→TPR2) takes place. The first TPR is shown in blue and reaches a final steady state value of 2.77 absorbance units and reaches its maximum 5 minutes before the TPR2 reaction. This is in line with the MS data showing that the time of consumption of hydrogen increased from TPR1 to TPR2 by 5 minutes. This suggests that the absolute value of the absorbance can be directly related to the extent of reduction of the catalyst. As the catalyst becomes more reduced, the absorbance units increase.

Also, the maximum value of the absorbance units decreased from 2.77 to 2.63 for TPR2. This supports the previously discussed results of incomplete reversibility for the reaction. If the reaction were fully reversible, the hydrogen consumptions during TPR1 and TPR2 would be the same and the absorbance lines should line up.

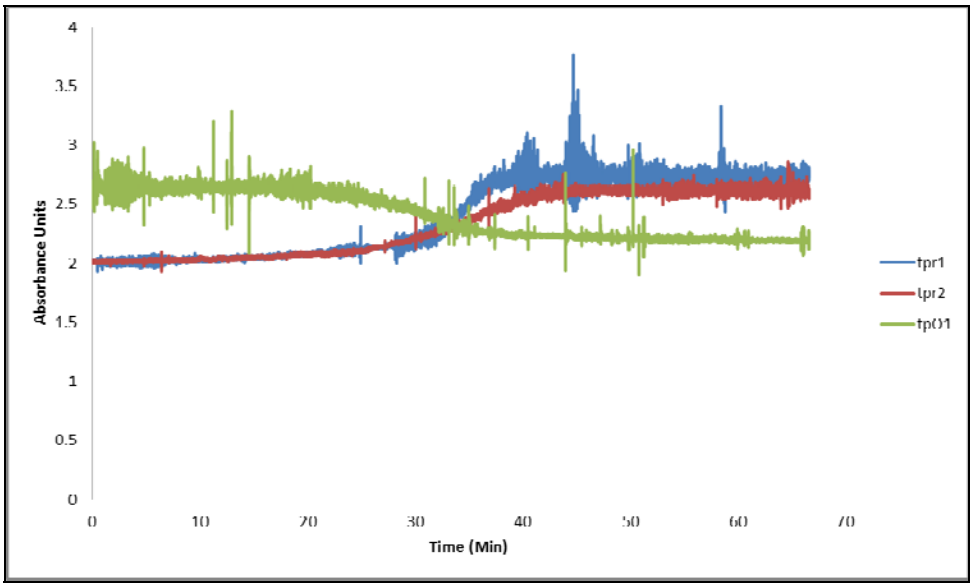

Figure 27 Varian Kinetics program at 800 nm TPR and TPO for 1 wt% lanthana catalyst.

The slopes of the lines for the TPR/TPO spectra appear to have a direct correlation to the rate of reduction or oxidation; with the steeper slopes having higher rates of consumption than the shallower slopes. The consumption rates in (mol $gcat^{-1}$ min^{-1}) are shown below in Figure 28.

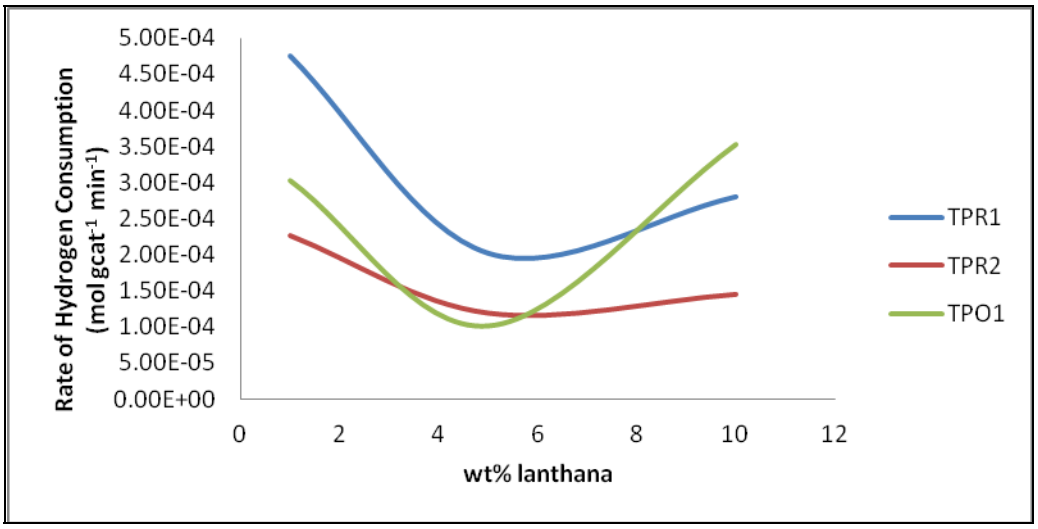

Figure 28 Rates of consumption for TPRs and TPO.

The slope of TPO1 from the Kinetics® program for the 10 wt% lanthana catalyst is slightly steeper than the 1 wt% lanthana catalyst (-0.025 compared to -0.02). The oxygen consumption rates in terms of (mol $gcat^{-1}$ min^{-1}) is slightly higher for the 10 wt% lanthana catalyst compared to the 1 wt% lanthana catalyst. While the rate of oxygen consumption is not relevant to WGS activity, the concept that the rates of the reaction can be correlated to the slopes of the UV-Visible spectra is valuable. This will allow for future studies to correlate the activity of the catalyst to the UV-Visible spectra obtained from the catalyst surface.

The TPR and TPO graphs for the 5 wt% lanthana catalyst (Figure 29) still show many similarities to the 1 wt% lanthana catalyst. The TPR's both increase and the TPO decreases. All of the TPR and TPO graphs show this correlation. This shows that absorbance is responsive to the overall extent of reduction in the system. This response in absorptivity is the foundation for the overall extent of reduction calculation. The amount of change in absorbance can then be directly related to amount of hydrogen or oxygen (TPR/TPO) consumed by the catalyst during

reduction. This then serves as a baseline for calculating the extent of reduction in the system during WGS conditions.

The TPR1 still goes slightly higher than TPR2; however the steady state absorbance difference for the 5 wt% lanthana TPRs is significantly smaller than the gap for the 1 wt% lanthana TPR; 2.75 to 2.7 for TPR1 to TPR2 compared to the 0.14 absorbance units difference in TPR1.

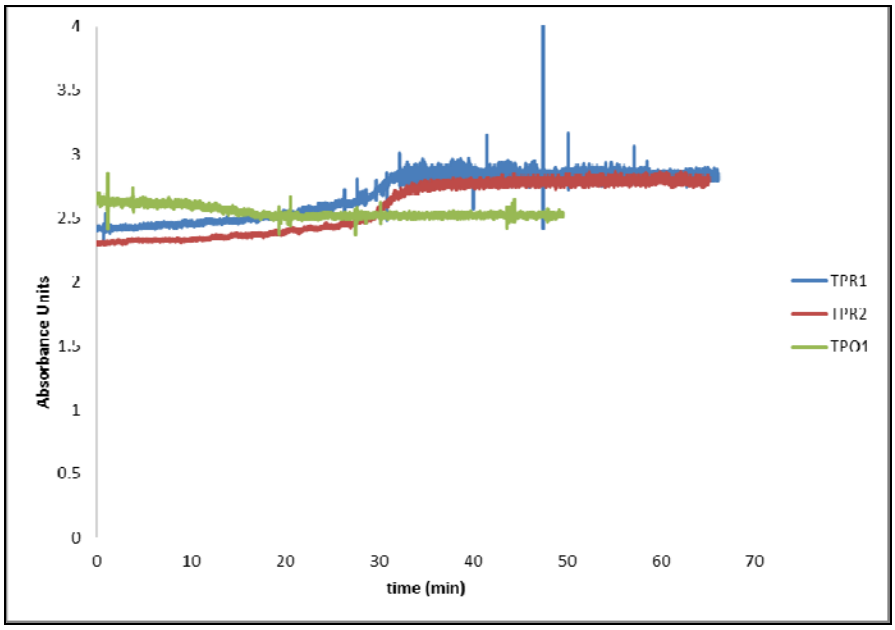

Figure 29 TPR TPO for 5 wt% lanthana catalyst via kinetics program.

Where these two differ is in the TPO; while the 1 wt% lanthana catalyst has a definite "S" curve shape to its TPO, the 5 wt% lanthana catalyst has a much more gradual descent before it reaches steady state absorbance level. This might suggest that the 5 wt% lanthana catalyst is less active than the 1 wt% lanthana catalyst (as the WGS kinetic data show in Section 5.2.1). Another reason for this could be the lanthanum's ability to facilitate oxygen desorption. The

TPO is attempting to reincorporate an oxygen molecule into the iron oxide lattice; however, if that oxygen desorbs before it can be properly bonded into the lattice structure, it would slow the rate of oxygen consumption by the catalyst.

Section 1.4 explains that a possible effect of lanthanum is the facilitation of desorption of oxygen species from the iron catalyst. This would also suggest that it is more difficult to adsorb oxygen species onto the iron surfaces, making the TPO more difficult and therefore a more gradual process.

Figure 30 shows the 10 wt% lanthana catalyst. These data continue the trend shown between 1 wt% lanthana and 5 wt% lanthana because the TPO is significantly more gradual in decline of absorbance units than the 1 wt% lanthana catalyst. The steady state absorbance unit values are nearly identical after TPR1 and TPR2 (2.35 and 2.34 absorbance units for TPR1 and TPR2, respectively).

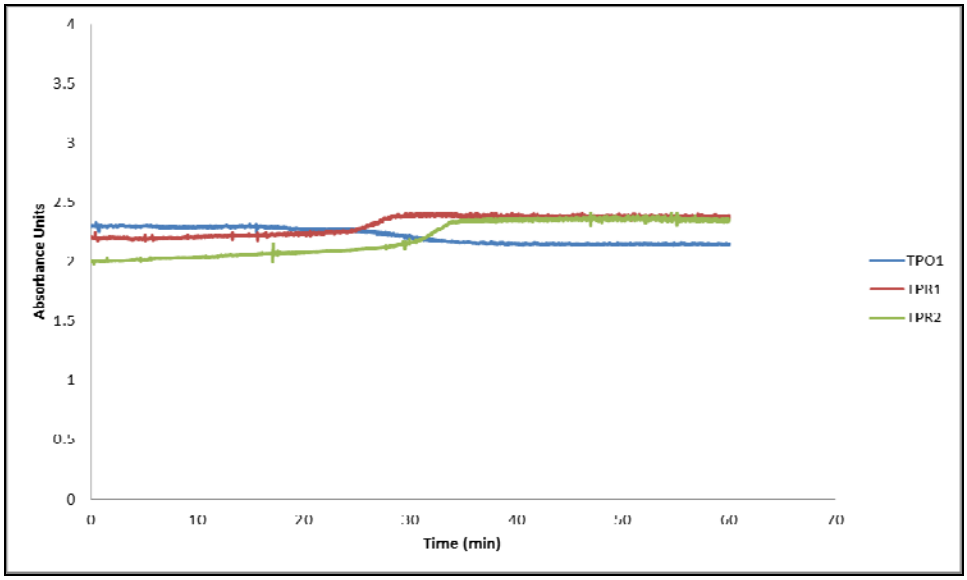

Figure 30 TPR/TPO kinetics program of 10 wt% lanthana catalyst.

Another measure of activity in these catalysts is the overall change in absorbance from start to finish. The 1 wt% lanthana catalyst has a change from 2 to 2.77, the 5 wt% lanthana catalyst changes from 2.3 to 2.75, while the 10 wt% lanthana catalyst changes from 2 to 2.35 absorbance units. As the lanthana percentage increases, the overall change in the absorbance units decreases, suggesting that there is less change in the catalyst during the TPR1 as lanthana increased. In other words, as lanthana is increased, the reduction activity of the catalyst decreased.

3.3.4 TPR and TPO Analysis via UV-Visible Scan® Program

Following the experimental method outlined in Section 3.2.4 Data Gathering Procedure for the UV-Visible In-situ Reactor, each of the seven steps outlined has a UV-Vis scan taken after it. These scans measure absorbance as a function of wavelengths of light from the visible region (12,500 cm^{-1} wavenumbers) to the UV region (50,000 cm^{-1} wavenumbers). For the 1 wt% lanthana catalyst, the scans following the first five procedure steps are shown in Figure 31. Each of the procedure steps mentioned, TPR1, TPR2, etc. was performed prior to the scan. These spectra represent an overall change in the absorbance of the catalyst after the reactions have taken place.

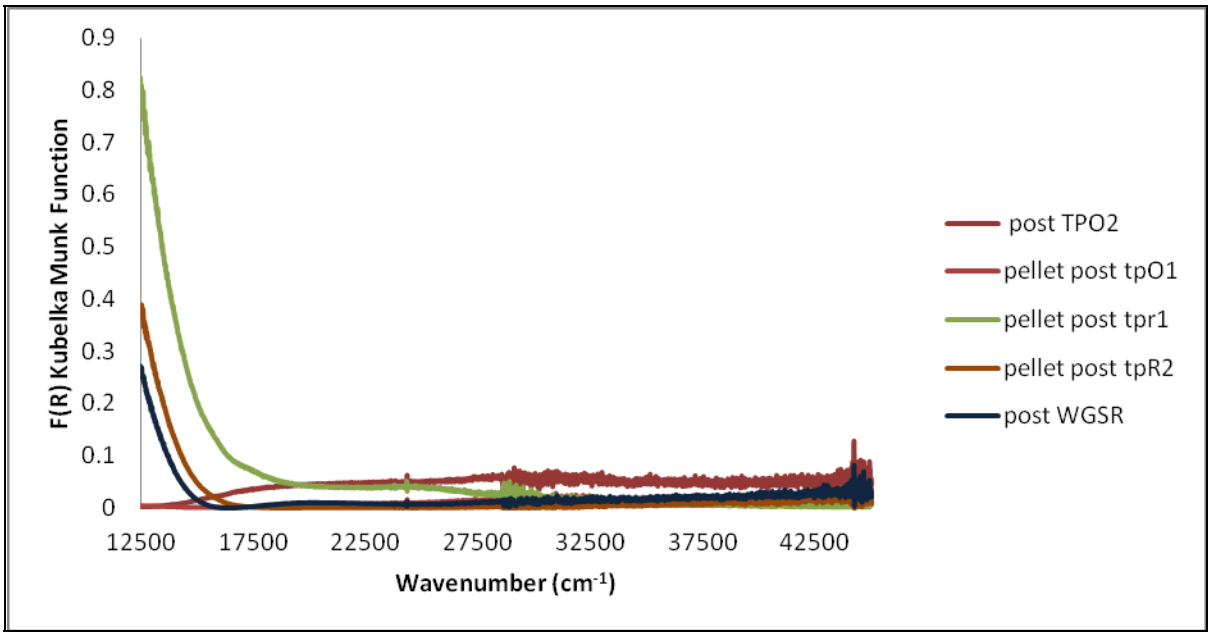

Figure 31 TPR/TPO Scans for 1wt% lanthana catalyst. Scans were taken after each of the steps.

Figure 31 shows the significant change in signal at the 12,500 wavenumber frequency. This area of the spectra shows the most change in absorbance; because of this, the 12,500 wavenumber frequency was used in the kinetics scans in the previous section. The first step procedurally is TPR1, which has the highest overall Kubelka Munk value at 0.85. This is expected because the greatest change in the catalyst should occur when the catalyst is fresh and has not had a chance to deactivate.

Following TPR1, TPO1 is a relatively flat baseline along the x-axis. This suggests that the catalyst was successfully re-oxidized to its initial oxidation state. If the Kubelka Munk Function (F(R)) reference and the data to which this baseline is being compared to are exactly equal, then the resulting F(R) output should be the x-axis. TPR2 however, only increases to a maximum value of 0.4. This relates back to the previous discussion on reversibility of the absorptivity of the catalyst, in that if the catalyst absorbance were fully reversible TPR1 and

TPR2 should line up directly on top of each other. Therefore, there is a direct correlation to the F(R) value of a scan and the extent of the reaction taking place. Likewise, although TPO2 no longer overlays the x-axis, the difference is considered negligible, with the second reoxidized scan running virtually parallel to the x-axis at a slightly higher value of 0.06.

The last step before the WGS condition is the water gas shift reduction condition. This step is unlike a TPR in that it attempts to maximize the magnetite content of the catalyst prior to WGS conditions. Also, this is the first time water and CO are added to the system. This combination of oxidizing (H_2O) and reducing (CO) agents in the inlet stream during these conditions help prevent the WGS reduction reaction from moving as high in F(R) units as the TPR's. This proves to be the case, as shown above. However, the shape of the WGS reduction is the same shape as TPR1 and TPR2, suggesting that the majority of the reaction taking place is the reduction of Fe_2O_3 to Fe_3O_4, like in the TPR's, since multiple peaks are not observed that would correspond to reduction to FeO or Fe that are expected to take place at higher temperatures (Gunugunuri 2011).

Following the WGS reduction conditions, WGS conditions are immediately started in the system. Figure 32 Scan results for 1wt% lanthana catalyst under WGS conditions shows how the spectra changes during the WGS reaction. As time under WGS conditions increases, the F(R) values increase, suggesting that the catalyst is undergoing further reduction. These are the data that permit the extent of reduction calculation.

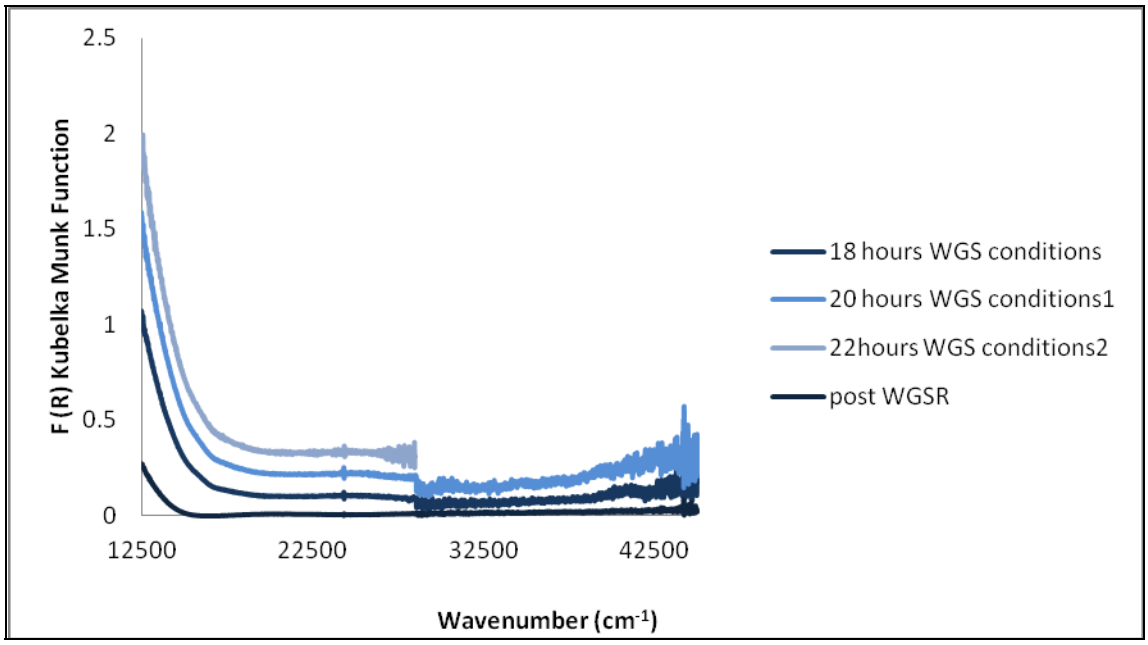

Figure 32 Scan results for 1wt% lanthana catalyst under WGS conditions.

Below is a side by side comparison of Figure 19 and Figure 32. The lower frequency wavelengths for both are increasing as a function of time in the system. On the left, the increasing F(R) values at the 625 nm wavelength signified the increase in Cr^{3+} production. Likewise the increase at the 12,500 wavenumber or 800 nm wavelength on the right demonstrates the extent of reduction of the Fe_3O_4 catalyst during WGS conditions. However, due to the rapid physical expansion of the catalyst when exposed to water (as discussed in section 3.1.8 Structural Stability in the UV-Visible In-situ Reactor), the catalyst does not maintain its surface long enough to reach a steady state absorbance value.

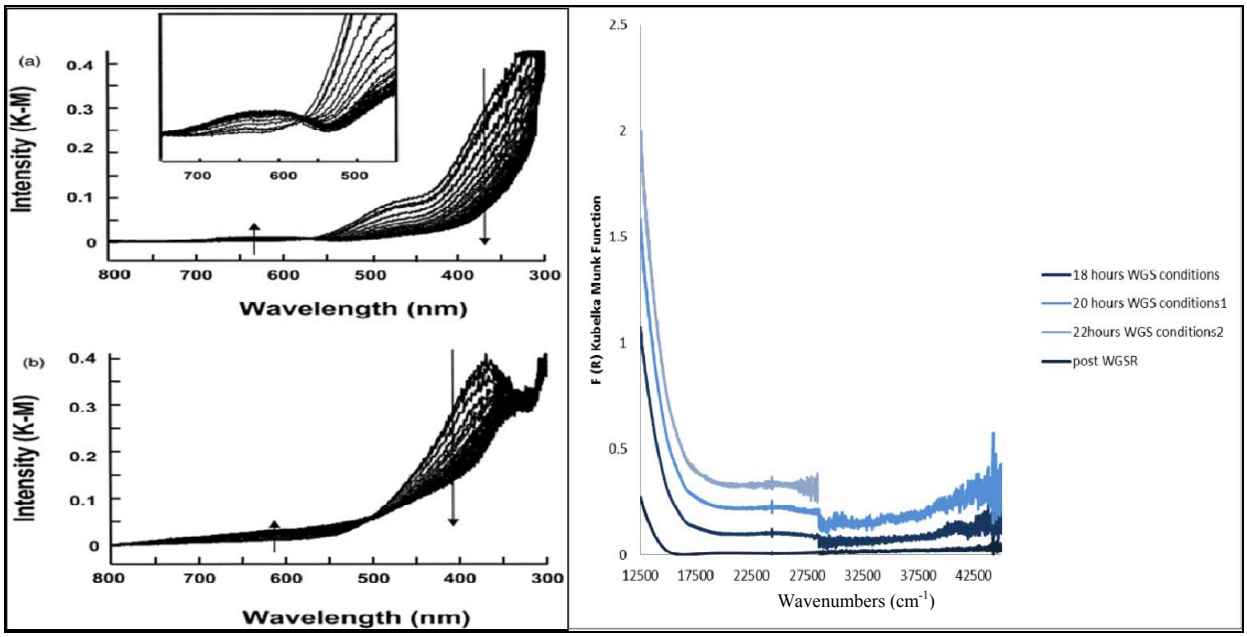

Figure 33 Side by side view of Figure 19 and Figure 32 for comparison.

Without a steady state absorbance value for the catalyst, a definite edge energy cannot be accurately determined, and the techniques described in Section 3.1.5 Edge and Pre-Edge Energies cannot be used. One of the major recommendations for future work is to resolve this issue.

3.3.5 Extent of Reduction of 1 wt% Lanthana Catalyst Using UV-Visible Spectra

Taking the value of the Figure 32 scans at 12,500 wavenumbers (the frequency that showed the most signal), and comparing the results with the amount of oxygen removed from the lattice during the TPRs, gives the data shown in Figure 34. As discussed in Section 3.3.3, the TPRs show the relative change in absorbance is sensitive to the oxidation state of the catalyst. By normalizing the absorbance data via the Kubelka Munk function and comparing the different absorbances at different times during the WGS process, an overall extent of reduction of the iron

in the catalyst can be determined at any given point in the reaction process. The blue diamonds in Figure 34 represent the TPR/TPO data while the red boxes represent F(R) values for the WGS conditions.

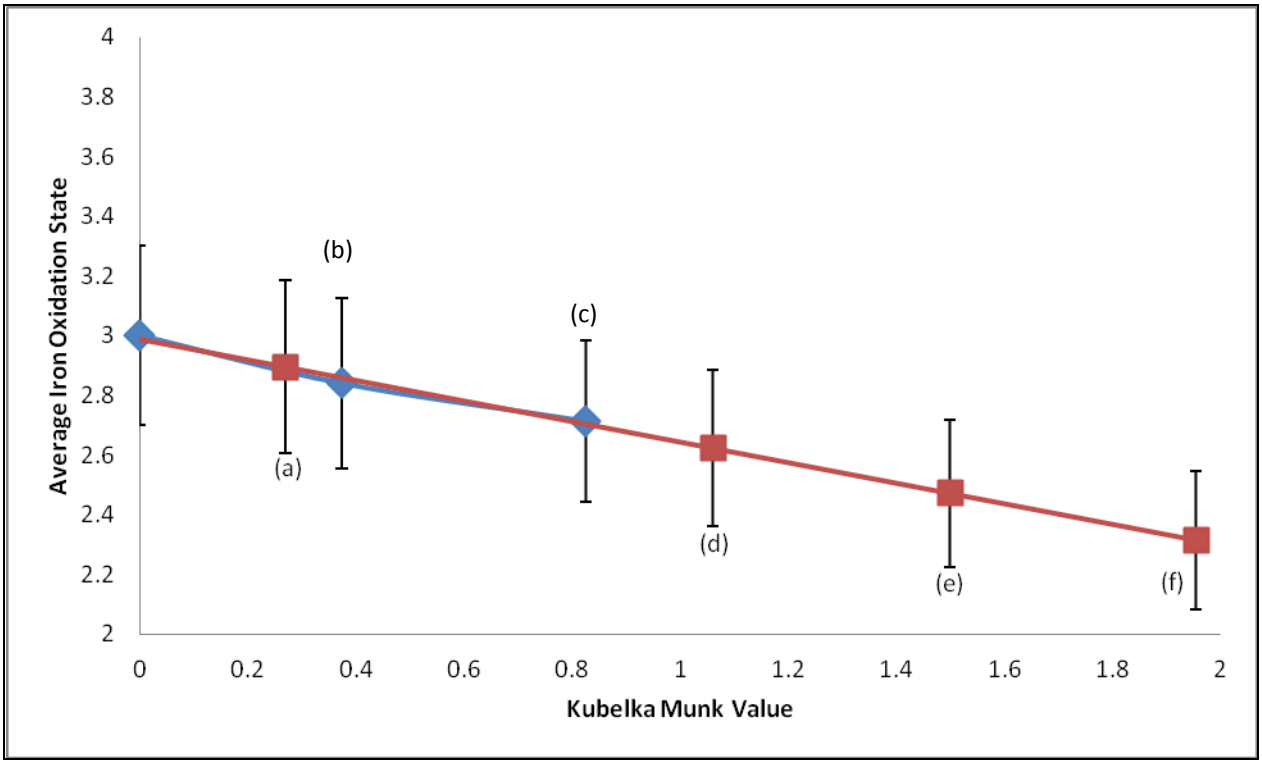

Figure 34 Overall extent of teduction for 1 wt% lanthana catalyst a) post WGS pretreatment conditions. b) post TPR2 c) post TPR1 d) 18 hours WGS conditions e) 20 hours WGS conditions f) 22 hours WGS conditions.

A y-axis value of 2.7 implies that 1/9 of the original oxygen atoms in the lattice have been removed, or that on average, a complete reduction from Fe_2O_3 to Fe_3O_4 has occurred. This 1/9 of the original oxygen atoms could have been removed in such a way that a combination of oxidation states are possible in the system, i.e. mostly Fe_3O_4 but a balance of Fe_2O_3 and FeO could lead to the same average iron oxidation state of 2.7+. However, for the duration of this discussion, an average iron oxidation state of 2.7+ will be assumed to correspond to complete

conversion to Fe_3O_4. This assumption is supported by the TPR data, which show only a single peak over the temperature range described. The red datum point that corresponds to the Fe^{3+} to $Fe^{2.7+}$ reduction is the 18 hours of WGS conditions point. This shows that the catalyst has its highest concentration of active phase iron at approximately 18 hours of reaction conditions. Also, as the reaction time increases, the oxidation state of the catalyst continues to decline to $Fe^{2.4+}$ in a matter of 4 hours from the $Fe^{2.7+}$. This is a very rapid consumption of the active phase in the catalyst. However, this is consistent with the high deactivation percentages (20-40% deactivation in 5 days of use) shown in Section 2.3. Originally, this deactivation was attributed to sintering; however, this extent of reduction data seem to suggest that loss in active phase could be attributed to over-reduction of the catalyst under WGS conditions to FeO. Metallic iron is not likely to be formed for two reasons. First, a much higher temperature (~590°C) is generally required to reduce to the metal (Longbottom and Kolbeinsen). Second, metallic iron is an effective methanation catalyst, but no methane was detected in the reaction products. Although over-reduction is not expected during normal industrial WGS reaction conditions, the amount of reactant water added during this optical study was limited to about 2:1 H_2O:CO to avoid condensation in the reactor cell, while a more typical industrial value, and the one used for the kinetic experiments is 3:1. The smaller than normal quantity of water in the system could lead to reaction conditions favorable for over-reduction of the catalysts. However, these preliminary data must be confirmed during future work.

3.4 Conclusions

The objective of this work was to characterize the potential benefits of the addition of lanthanum oxide (lanthana) to the iron-chromium-copper (Fe-Cr-Cu) oxide catalysts industrially used in high temperature water gas shift processes via UV-Visible analysis as well as kinetic

analysis. Even though these iron oxide catalysts appear black to the eye, they do show a response in the UV-visible region when referenced to the fully-oxidized catalyst. Thus, this signal is interpreted as a change in absorbance from the catalysts fully oxidized state. This change in absorbance due to changes in the oxidation states of the iron on the surface of the catalyst leads to a direct calculation of overall extent of reduction in the catalyst. The 1 wt% lanthana catalyst shows that after 18 hours of WGS conditions, the iron has reduced from Fe_2O_3 to Fe_3O_4 and subsequently that the reduction from Fe_3O_4 to $Fe^{2.4+}$ takes place in the following 4 hours. Industrial WGS catalysts without lanthana take significantly longer (scale of days as opposed to hours) to reduce past the active $Fe^{2.7+}$ phase (Hla 2009). This suggests that the small lanthana addition (1 wt%) to the catalyst increases the activity at higher temperatures and also increases the reducibility of the catalyst. Even with the slight increase in activity, the generally lower thermal stability indicates that a lanthana addition is likely not suitable for industrial catalysts. However, this experiment was done with less water than industrial applications, which could account for the over reduction of the catalyst. While more testing will be required to determine if the addition of lanthana in WGS catalysts will be beneficial to industrial operations, the technique of measuring extent of reduction using UV-Vis spectroscopy, with a catalyst that is mostly black will prove to be useful in future catalytic work. Another possible explanation for the apparent over-reduction is carbon deposition on the surface of the catalyst. Although this is not expected, even at the 2:1 H_2O:CO feed conditions, a simple TPO must be conducted after the WGS conditions to verify that no CO_2 is formed.

Chapter 4 Future Work

Overall extent of reduction was determined via UV-Visible spectrocopic analysis during WGS conditions. However, the reaction did not reach steady state due to the physical expansion of the catalyst described in Section 3.1.8. Once this is resolved, and a steady state UV-Vis spectra can be taken, an edge energy can be determined (steady state absorbance value) and an analysis based on pre-edge energies (transient region) can be conducted to determine extent of reduction of the catalyst at any point in the system. Ideally, a catalyst of unknown reduction can be put analyzed by a simple UV-visible spectrum scan to quantify the oxidation states of its various components.

The UV-Vis experimental design requires multiple runs to determine if the rate of reduction of the lanthana doped catalysts is as rapid as determined in this study. Due to the intricate and delicate procedures involved in UV-Vis data collection, only a single run of the WGS conditions was successfully taken. That run did not have enough time to equilibrate before the physical expansion of the catalyst under WGS conditions ruined the surface. Therefore, there are significant uncertainties in the results of the extent of reduction calculation. Currently, through propagation of errors analysis, the error is estimated to be no less than 10% for the UV-Vis data. This will be improved through better control of the variables in the UV-Vis system, including maintaining a constant catalyst surface, as any small pressure spike in the inlet gas flow could move the surface of the catalyst enough to skew the results. Also, the thermocouple

measuring the temperature on the surface needs to be placed in a more controlled way. Currently, the thermocouple sits at varying angles and with varying contact with the catalyst, which would distort the actual temperature readings on the surface, which may be a contributing factor to over-reduction of the catalyst. Also, a more accurate measure of inlet water needs to be used to verify the extent of reduction shown in Figure 34. The water inlet ideally should be at a 3:1 ratio of H_2O:CO (the current value is about 2:1). All of these sources of error could significantly increase the reduction rate of the catalyst during WGS conditions, suggesting that the longevity of the lanthana catalysts is longer than what was indicated by the UV-visible study. If that proves to be the case, then the lanthana catalysts could prove to be effective in an industrial setting.

This study has shown that the addition of 1 wt% lanthana increases the WGS activity at higher temperatures. To verify this, a more complete characterization of the catalyst needs to be performed. This includes an XRD analysis of the lattice structure. XRD has the ability to determine lattice structure of the crystal domains of a given catalyst. Unit cell dimensions, lattice symmetry, crystallinity, and crystallite sizes can all be determined with XRD (Perego 1998). While XRD does give extensive information regarding the bulk properties of a material, it gives very little information at the surface of the material. XRD characterization will be performed to determine if crystallinity and crystallite size of the as-prepared and the used catalysts have an effect on the kinetics of the system. Also, XRD will verify if the preparation method of the catalyst results in the solid solution of components that was assumed in this study. Eventually, XANES spectra should also be taken in order to confirm the extent of reduction results obtained by UV-visible spectroscopy against the demonstrated XANES method.

Finally, the rate law and mechanism of the reaction on these catalysts should be determined. First, a simple power law rate analysis of the catalysts should be performed to better

model the kinetics of the system. This should be followed by a Langmuir-Hinshelwood microkinetic model analysis of the rate based on a sequence of elementary steps.

References

Argyle, M. D., Chen, K., Resini, C., Krebs C., Bell A. T., and Iglesia E. (2004). "Extent of reduction of vanadium oxides during catalytic oxidation of alkanes measured by in-situ UV−Visible spectroscopy." *The Journal of Physical Chemistry B* 108, no. 7: 2345.

Bartholomew, C. H. c2006. *Fundamentals of industrial catalytic processes*. Ed. Robert J. Farrauto 1941. 2nd ed. ed.Hoboken, N.J.: John Wiley.

Berry, A. J., Yaxley, G. M., Woodland, A.B., and Foran, G.J. (2010). "A XANES calibration for determining the oxidation state of iron in mantle garnet." *Chemical Geology* 278, no. 1-2: 31-37.

Catalyst handbook 1989. Ed. ltd Imperial Chemical Industries. London: London : Wolfe.

Chinchen, G. C., Logan, R. H. and Spencer, M. S. (1984). "Water-gas shift reaction over an iron oxide/chromium oxide catalyst. II: Stability of activity." *Applied Catalysis* 12, no. 1: 89-96.

Christy, A. A., Kvalheim, O. M., and Velapoldi, R. A. (1995). "Quantitative analysis in diffuse reflectance spectrometry: A modified kubelka-munk equation." *Vibrational Spectroscopy* 9, no. 1: 19-27.

Doppler, G., Trautwein, A. X., Ziethen, H. M., Akmbach, E., Lehnert, R., Sprague, M. J., and Gonser, U. (1988). "Physical and Catalytic Properties of High-Temperature Water-Gas Shift Caatalysts Based upon Iron-Chromium Oxides." *Applied Catalysis* 40, no. 1-2: 119-130.

Edwards, M. A. and W (2002). "Microstructural studies of the copper promoted iron oxidechromia water-gas shift catalyst." *Physical Chemistry Chemical Physics,* Vol.4, no. 15: 3902-3908.

Gunter, K. K., Miller, L. M., Aschner, M., Eliseev, R., Depuis, D., Gavin, C. E., and Gunter, T.E. (2002). "XANES spectroscopy: A promising tool for toxicology: A tutorial." *Neurotoxicology* 23, no. 2: 127-146.

Gunugunuri K. R., Gunasekara, K., Boolchand, P., and Smirniotis, P. G. (2011). "Cr- and ce-doped ferrite catalysts for the high temperature Water−Gas shift reaction: TPR and mossbauer spectroscopic study." The journal of physical chemistry C 2011 *115* (4), 920-930.

Harrick Scientific. Harrick praying mantis cell. Harrick Scientific. http://www.harricksci.com/ftir/accessories/group/Praying-Mantis%E2%84%A2-Diffuse-Reflection-Accessory (accessed Mar 30, 2012).

Herranz, T., Rojas, S., Perez-Alonso, F., Ojeda, M., Terreros, P., and Fierro, J. L. G. (2006). "Carbon oxide hydrogenation over silica-supported iron-based catalysts. influence of the preparation route." *Applied Catalysis A: General* 308, : 19-30.

Hla, S. S., Park, D., Duffy, G. J., Edwards, J.H., Roberts, D. G., Ilyushechkin, A., Morpeth, L.D. and Nguyen, T. (2009). "Kinetics of high-temperature water-gas shift reaction over two iron-based commercial catalysts using simulated coal-derived syngases." *Chemical Engineering Journal* 146, no. 1: 148-154.

Hla, S. S., Sun, Y., Duffy, G. J., Morpeth, L. D., Ilyushechkin, A., Cousins, A., Roberts, D. G., and Edwards, J. H. (2011). "Kinetics of the water-gas shift reaction over a La0.7Ce0.2FeO3 perovskite-like catalyst using simulated coal-derived syngas at high temperature." *International Journal of Hydrogen Energy* 36, no. 1: 518-527.

Hu, Y., Jin, H., Liu, J., and Hao, D (2000). "Reactive behaviors of iron-based shift catalyst promoted by ceria." *Chemical Engineering Journal* 78, no. 2-3: 147-152.

Longbottom, R., Kolbeinsen, L. (2008). "Iron ore Reduction with CO and H2 Gas Mixtures – Thermodynamic and Kinetic Modelling." New Direct Reduction, Proceedings of the 4th Ulcos Seminar, October 2008.

Perego, G. (1998). "Characterization of heterogeneous catalysts by X-ray diffraction techniques." *Catalysis Today* 41, no. 1-3: 251-259.

Ramachandran, R. and Menon, R. K. (1998). "An overview of industrial uses of hydrogen." *International Journal of Hydrogen Energy* 23, no. 7: 593-598.

Rhodes, C. (2003). "Studies of the role of the copper promoter in the iron oxide/chromia high temperature water gas shift catalyst." *Phys. Chem. Chem. Phys* 5, : 2719-2723.

Rhodes, C., Williams, B. P., King F., and Hutchings, G. J. (2002). "Promotion of Fe3O4/Cr2O3 high temperature water gas shift catalyst." *Catalysis Communications* 3, no. 8: 381-384.

Sato, T., Kurosawa, S., Smith, R. L., Adschiri, T., and Arai, K. (2004). "Water gas shift reaction kinetics under noncatalytic conditions in supercritical water." *The Journal of Supercritical Fluids* 29, no. 1-2: 113-119.

Sherman, D. M. (2008). "Oxide and hydroxide minerals." *In AccessScience, ©McGraw-Hill Companies*.

Sinfelt, J. H. (2002). "Role of surface science in catalysis." *Surface Science* 500, no. 1-3: 923-946.

Sun, Y., Hla, S. S., Duffy, G. J., Cousins, A. J., French, D., Morpeth, L. D., Edwards, J. H., and Roberts, D. G. (2011). "Effect of Ce on the structural features and catalytic properties of la(0.9−x)CexFeO3 perovskite-like catalysts for the high temperature water–gas shift reaction." *International Journal of Hydrogen Energy* 36, no. 1: 79-86.

Varian Corp. Varian Cary 4000 UV-visible spectrometer. Varian Corporation. http://www.varianinc.com.cn/products/spectr/uv/brochure/1942.pdf (accessed Sep 25, 2010).

Wachs, I. E. (2005). "Recent conceptual advances in the catalysis science of mixed metal oxide catalytic materials." *Catalysis Today* 100, no. 1-2: 79-94.

Weckhuysen, B. M. and Schoonheydt, R. A. (1999). "Recent progress in diffuse reflectance spectroscopy of supported metal oxide catalysts." *Catalysis Today* 49, no. 4: 441-451.

Weckhuysen, B. M., Verberckmoes, A. A., Debaere, J., Ooms, K. Langhans, I. and Schoonheydt, R. A. (2000). "In situ UV–Vis diffuse reflectance spectroscopy — on line activity measurements of supported chromium oxide catalysts: Relating isobutane dehydrogenation activity with Cr-speciation via experimental design." *Journal of Molecular Catalysis A: Chemical* 151, no. 1-2: 115-131.

Xue, E., O'Keeffe, M., and Ross, J. R. H. (1996). "Water-gas shift conversion using a feed with a low steam to carbon monoxide ratio and containing sulphur." *Catalysis Today* 30, no. 1–3: 107-118.

Zhao, H., Hu, Y., and Li, J. (1999). "Reduced rate method for discrimination of the kinetic models for the water–gas shift reaction." *Journal of Molecular Catalysis A: Chemical* 149, no. 1–2: 141-146.